2019

Computational Study of Water Desalination Using Direct Contact Membrane Distillation

Anas Mohammed Alwatban
Lehigh University

Computational Study of Water Desalination Using Direct Contact Membrane Distillation

by

Anas Mohammed Alwatban

Presented to the Graduate and Research Committee

of Lehigh University

in Candidacy for the Degree of

Doctor of Philosophy

in

Mechanical Engineering

Lehigh University

May 2019

SAMPLE DISSERTATION SIGNATURE SHEET

Approved and recommended for acceptance as a dissertation in partial fulfillment of the requirements for the degree of Doctor of Philosophy.

_____
Date

_____
Dissertation Director: Dr. Alparslan Oztekin

_____
Accepted Date

Committee Members:

_____
Committee Chair: Dr. Alparslan Oztekin

_____
Dr. Jacob Kazakia

_____
Dr. Edmund Webb

_____
Dr. Xuanhong Cheng

ACKNOWLEDGMENT

I would like to thank my father Mohammed Alwatban and my mother Roqayah Alwatban for their endless love and support, and I dedicate this work to them. God bless them now and forever. I am also grateful to my wife, Arwa Alwatban, who devoted all her time for me during my graduate studies.

I would like to express my deepest appreciation to my supervisor, Prof. Alparslan Oztekin, for his encouragement and valuable advice. Prof. Alparslan Oztekin has set an example of excellence as an instructor, researcher, and role model. I would also like to extend my gratitude to my Ph.D. committee members, Professor Jacob Kazakia, Professor Edmund Webb, and Professor Xuanhong Cheng for all of their time, guidance, and discussion through my PhD study. I also had great pleasure of working with Dr. Ahmed Alshwairekh for his insightful suggestions during my research.

Contents:

ACKNOWLEDGMENT III

CONTENTS: IV

LIST OF TABLES VI

LIST OF FIGURES VII

NOMENCLATURE X

ABSTRACT 1

CHAPTER 1: INTRODUCTION 3

Literature Review 7

CHAPTER 2: MATHEMATICAL MODEL 13

CHAPTER 3: A PARAMETRIC STUDY - EFFECT OF MEMBRANE PROPERTIES AND OPERATIONAL PARAMETERS 19

Numerical Model, Convergence, and Validation 19

Results 23

Conclusion 33

CHAPTER 4: THE PERFORMANCE CHARACTERISTICS OF DCMD MODULE CONTAINING SPACERS IN CHANNELS 35

Numerical Model and Convergence 35

Results and Discussion 39

Conclusion 47

CHAPTER 5: CHARACTERIZING PERFORMANCE OF THE EMBEDDED-SPACER MEMBRANES IN DIRECT CONTACT MEMBRANE DISTILLATION MODULES 49

Numerical Model, Convergence, and validation 49

Results 53

Conclusion 68

CHAPTER 6: LES SIMULATION IN DCMD MODULE CONTAINING SPACERS 70

Mathematical model 70

Results 71

Conclusion 75

CHAPTER 7: CONCLUSION 77

REFERENCES 81

VITA 90

List of Tables

Table 1. Permeability models 16
Table 2. The permeation flux predicted and measured for various values of the feed channel Re 22
Table 3. Membrane parameters used in the simulations 23
Table 4. Knudsen number values for the selected pore sizes 25
Table 5. Feed operating parameters used in the simulations 30
Table 6. Membrane properties and operating parameters 36
Table 7. The area-averaged concentration and temperature polarization coefficients, maximum shear stress, and the water flux in the module with and without spacers at various values of the feed stream Ref 46
Table 8. Energy balance and pumping power for the DCMD system 47
Table 9. Membrane properties and operating parameters used in the simulations 51
Table 10. membrane properties for the two membranes used in the experimental work done by [13] 54
Table 11. The area-averaged concentration and temperature polarization coefficients, maximum shear stress, and the water flux $(J: kg\ m-2h-1)$ in the module with and without embedded spacers at various feed and permeate flow rates. 68

List of Figures

Figure 1. Schematic diagram of the DCMD process 6

Figure 2. Profiles of a) the stream-wise component of the velocity at z/h = 2.5 and x/h = 25, b) the normalized concentration over the surface of the membrane in the feed side at z/h = 2.5, and c) the normalized temperature over the surface of the membrane in the feed and permeate side at z/h = 2.5. The profiles are acquired using the mesh density of N1 = 1 million, N2 = 1.6 million, N3 = 3.2 million, and N4 = 6.4 million elements. 22

Figure 3. The area-averaged water flux for various values of the membrane thickness and the porosity of a) pore size = 0.20 µm, b) pore size = 0.45 µm, and c) pore size = 1 µm. 25

Figure 4. The area-averaged temperature polarization coefficient for various values of the membrane thickness and the porosity of a) pore size = 0.20 µm, b) pore size = 0.45 µm,and c) pore size = 1 µm 27

Figure 5. The area-averaged concentration polarization coefficient for various values of the membrane thickness and the porosity of a) pore size = 0.20 µm, b) pore size = 0.45 µm, and c) pore size = 1 µm. 29

Figure 6. The area-averaged a) water flux, b) temperature polarization coefficient, c) concentration polarization coefficient as a function of the inlet feed temperature. 31

Figure 7. The area-averaged a) water flux, b) temperature polarization coefficient, c) concentration polarization coefficient as a function of the feed flow rate 33

Figure 8. Schematics of the module containing net-type spacers and dimensions of the geometry. 37

Figure 9. Profiles of a) the stream-wise component of the feed velocity at z/h = 2 and y/h = 0.9, b) the normalized concentration over the surface of the membrane at the feed side at z/h = 2, and c) the normalized temperature over the surface of the membrane at the feed and the permeate sides at z/h = 2. The profiles are acquired using the mesh density of M1, M2, M3, and M4. 38

Figure 10.A sample of the unstructured mesh for the geometry with net-type spacers. 39

Figure 11. Contours of the normalized stream-wise feed velocity at y/h = 0.9 for a) Ref = 500 and d_s = 0.25h, b) Ref = 500 and d_s = 0.5h, c) Ref = 1500 and d_s = 0.25h, d) Ref = 1500 and d_s = 0.5h Images are rendered at 23 ≤ x/h ≤ 47. 40

Figure 12. Contours of the normalized temperature along the membrane surface at the feed side for a) Ref = 500 and d_s = 0.25h, b) Ref = 500 and d_s = 0.5h, c) Ref = 1500 and d_s = 0.25h, d) Ref = 1500 and d_s = 0.5h, and at the permeate side for e) Ref = 500 and d_s = 0.25h, f) Ref = 500 and d_s = 0.5h, g) Ref = 1500 and d_s = 0.25h, h) Ref = 1500 and d_s = 0.5h. Images are rendered at 23 ≤ x/h ≤ 47 at the feed side and 15 ≤ x/h ≤ 35 at the permeate side. 41

Figure 13. Contours of the normalized concentration along the membrane surface at the feed side for a) Ref = 500 and d_s = 0.25h, b) Ref = 500 and d_s = 0.5h, c) Ref = 1500 and d_s = 0.25h, d) Ref = 1500 and d_s = 0.5h.Images are rendered at 23 ≤ x/h ≤ 47. 43

Figure 14. Contours of the normalized wall shear stress at the feed side for a) Ref = 500 and d_s = 0.25h, b) Ref = 500 and d_s = 0.5h, c) Ref = 1500 and d_s = 0.25h, d) Ref = 1500 and d_s = 0.5h.Images are rendered at 23 ≤ x/h ≤ 47 44

Figure 15. Contours of the normalized water flux for a) Ref = 500 and d_s = 0.25h, b) Ref = 500 and d_s = 0.5h, c) Ref = 1500 and d_s = 0.25h, d) Ref = 1500 and d_s = 0.5h.Images are rendered at 23 ≤ x/h ≤ 47. 45

Figure 16. Schematics of the module containing embedded spacers and dimensions of the geometry. . 51

Figure 17. Profiles of a) the stream-wise component of the feed velocity at z/ h = 2 and y/h = 0.5, b) the normalized concentration over the surface of the membrane in the feed side at z/ h = 2, c) the

normalized temperature over the surface of the membrane in the feed side at z/ h = 2, and d) the normalized temperature over the surface of the membrane in the permeate side at z/ h = 2. 52
Figure 18. A sample of the unstructured mesh for the geometry with embedded spacers. 53
Figure 19. Contours of the normalized stream-wise velocity in the feed channel at y/h = 0.8 for a) Ref = 500 and D = 0.1h, b) Ref = 1500 and D = 0.1h, c) Ref = 500 and D = 0.2h, d) Ref = 1500 and D = 0.2h, e) Ref = 500 and D = 0.3h, f) Ref = 1500 and D = 0.3h. Images are rendered at 28 ≤ x/h ≤ 47. 56
Figure 20. Iso-surfaces of the normalized Q-criterion at a level of 0.01 plotted in the feed channel for a) Ref = 500 and D = 0.1h, b) Ref = 1,500 and D = 0.1h, c) Ref = 500 and D = 0.2h, d) Ref = 1,500 and D = 0.2h, e) Ref = 500 and D = 0.3h, f) Ref = 1,500 and D = 0.3h. Images are rendered at 31 ≤ x/h ≤ 40. 56
Figure 21. Contours of the normalized concentration along the membrane surface at the feed side a) Ref = 500 and D = 0.1h, b) Ref = 1500 and D = 0.1h, c) Ref = 500 and D= 0.2h, d) Ref = 1500 and D = 0.2h, e) Ref = 500 and D = 0.3h, f) Ref = 1500 and D = 0.3h Images are rendered at 28 ≤ x/h ≤ 47. 58
Figure 22. Profiles of the normalized concentration along the membrane surface at the feed side at z/h = 2 for Ref = 1500. Concentration profiles are acquired in the module containing spacers of strand diameter a) D = 0.1h, b) D = 0.2h, c) D= 0.3h and are compared to that obtained in the module containing membrane without embedded spacers. 59
Figure 23. Contours of the normalized temperature along the membrane surface at the feed side for a) Ref = 500 and D = 0.1h, b) Ref = 1500 and D = 0.1h, c) Ref = 500 and D= 0.2h, d) Ref = 1500 and D = 0.2h, e) Ref = 500 and D = 0.3h, f) Ref = 1500 and D = 0.3h Images are rendered at 28 ≤ x/h ≤ 47. 61
Figure 24. Profiles of the normalized temperature along the membrane surface at the feed side at z/h = 2 for Ref = 1500. Temperature profiles are acquired in the module containing spacers of strand diameter a) D = 0.1h, b) D = 0.2h, c) D= 0.3h and are compared to that obtained in the module containing membrane without embedded spacers 62
Figure 25. Contours of the normalized temperature along the membrane surface at the permeate side for a) $Rep = 330$ and D = 0.1h, b) $Rep = 1500$ and D = 0.1h, c) $Rep = 330$ and D = 0.2h, d) $Rep = 1500$ and D = 0.2h, e) $Rep = 330$ and D = 0.3h, f) $Rep = 1500$ and D = 0.3h. Images are rendered at 18 ≤ x/h ≤ 37 for $Ref = 1500$. 64
Figure 26. Profiles of the normalized temperature along the membrane surface at the permeate side at z/h = 2 for $Rep = 1500$ and $Ref = 1500$. Temperature profiles are acquired in the module containing spacers of strand diameter a) D = 0.1h, b) D = 0.2h, c) D= 0.3h and are compared to that obtained in the module containing membrane without embedded spacers. 65
Figure 27. Contours of the normalized wall shear stress at the feed side for a) Ref = 500 and D = 0.1h, b) Ref = 1500 and D = 0.1h, c) Ref = 500 and D= 0.2h, d) Ref = 1500 and D = 0.2h, e) Ref = 500 and D = 0.3h, f) Ref = 1500 and D = 0.3h Images are rendered at 28 ≤ x/h ≤ 47. The value of τmax (Pa) is a) 0.41, b) 1.3, c) 0.46, d) 1.5, e) 0.53, and f) 1.9. 66
Figure 28. Contours of the normalized water vapor flux for a) $Ref = 500$ and D = 0.1h, b) $Ref = 1500$ and D = 0.1h, c) $Ref = 500$ and D= 0.2h, d) $Ref = 1500$ and D = 0.2h, e) $Ref = 500$ and D = 0.3h, f) $Ref = 1500$ and D = 0.3h. Images are rendered at 28 ≤ x/h ≤ 47 for $Rep = 330$. 67
Figure 29. Contours of a) normalized feed concentration for steady flow b) normalized feed concentration for transient flow at α =28, c) normalized feed temperature for steady flow d) normalized feed temperature for transient flow at α =28, e) normalized feed wall shear stress for steady flow f) normalized feed wall shear stress for transient flow at α =28 g) normalized water flux for steady flow h) normalized water flux for transient flow at α =28. 73
Figure 30. Contours of Iso-surfaces of the Q criterion at level 0.06 of the feed channel for a) steady flow b) transient flow at α=28. 74

Figure 31. Contours of a) normalized feed concentration, b) normalized feed temperature, c) normalized feed wall shear stress, d) normalized water flux. All transient flow at α = 42 75

NOMENCLATURE

c	solute mass fraction	$kg_{solute}\, kg_{water}^{-1}$
c_p	specific heat of the water	$kJkg^{-1}K^{-1}$
d_p	membrane pore diameter	m
h_d	channel hydraulic diameter	m
k_w	thermal conductivity of water	$Wm^{-1}K^{-1}$
k_g	thermal conductivity of the gas	$Wm^{-1}K^{-1}$
k_m	thermal conductivity of the membrane	$Wm^{-1}K^{-1}$
k_s	thermal conductivity of the solid	$Wm^{-1}K^{-1}$
$\dot{m}$	mass flow rate of the feed water	$kg\ s^{-1}$
r	membrane pore radius	m
p	pressure	Pa
A	cross-sectional area of the feed channel	m^2
C	membrane permeability	$kg\ m^{-2}Pa^{-1}s^{-1}$
D	solute diffusion coefficient	m^2s^{-1}
D_v	diffusion coefficient of vapor	m^2s^{-1}
H_v	enthalpy of water vaporization	Jkg^{-1}
J	permeate flux	$kg\ m^{-2}s^{-1}$
K_B	Boltzmann constant	$m^2kgs^{-2}K^{-1}$
M_w	molecular weight of water	$kg\ mol^{-1}$
$\bar{P}$	average pressure within the membrane pores	Pa
P_a	pressure inside the membrane pore	Pa
P_v	vapor pressure	Pa
$\dot{P}$	Pumping power	W
$\dot{Q}_m$	total heat transfer through the membrane	Wm^{-2}
$\dot{Q}_f$	total thermal power input for the feed solution	Wm^{-2}
$\dot{Q}_c$	conduction heat transfer	Wm^{-2}
$\dot{Q}_v$	heat of vaporization	Wm^{-2}
R	universal gas constant	$m^2kg\ s^{-2}K^{-1}\ mol^{-1}$
Re	Reynolds number	$[-]$
T	temperature	K
$\vec{U}$	velocity vector	$m\ s^{-1}$
V_m	suction rate	$m\ s^{-1}$
Greek Letters		
ρ	density	kgm^{-3}
μ	viscosity	$Pa\ s$

λ	mean free path	m
σ	collision diameter of the water	m
δ	membrane thickness	m
τ	membrane tortuosity	$[-]$
ε	membrane porosity	$[-]$

Abstract

Computational fluid dynamics simulations were conducted to study the unit performance of direct contact membrane distillation for seawater desalination process in three-dimensional modules. A parametric study was conducted to assess the effects of the membrane properties and feed operational parameters on the flux performance and polarization characteristics of the module. Direct contact distillation membrane modules containing a net type of spacers in each channel were considered to promote mixing and thus to enhance performance. The novel design of spacers embedded within the membrane was introduced for polarization mitigation and performance enhance improvement at lower pressure losses. The laminar model was employed to describe the velocity, concentration and temperature field in the empty channels while the $k-\omega$ shear stress transport and LES (large eddy simulations) turbulence model were used in the module containing spacers. Dusty gas model is adopted for the mass diffusion through the membrane.

It was demonstrated that the membrane properties and operating parameters have a profound influence on the flux performance and the polarization characteristics. The water vapor flux increases as the thickness is decreased and the porosity and the pore size are increased. The intensity of temperature and concentration polarization are much greater at the higher inlet temperature of the feed solution. The increased feed flow rate improves the temperature and concentration polarization, but the polarization mitigation is limited when the flow regime in channels is laminar. The maximum flux obtained in the module without spacers was 64 $kg\ m^{-2}h^{-1}$ at membrane thickness of 100 μm, the porosity of 0.8, the pore size of 1 μm, inlet feed temperature of 80 ℃, and feed Reynolds number of 1500. The

overall module separation performance is improved in the module containing net-type spacers at all flow rates. Both water vapor flux, temperature polarization coefficient, and concentration polarization coefficient are improved with increasing spacer diameter. It is demonstrated that the presence of spacers in both channels enhances the membrane flux performance more than 50% and mitigate temperature and concentration polarization up to 30% at spacer diameter of $0.5h$ at flow rates. Although, the spacers become more efficient at a high flow rate and large spacer's diameter, the pressure drop increases with increasing the spacer's diameter. It is demonstrated that the novel design of the embedded spacers is very effective mitigating the temperature and concentration polarization and enhancing flux performance of the unit. The flux enhancement was 40% at the spacer's diameter of $0.3h$ and Reynolds number of 1500 for the feed and permeate streams. It is demonstrated here that spacers can be used effectively in direct contact membrane distillation modules to enhance performance and should be an integral part of the optimization and design of these separation systems.

Chapter 1: Introduction

Water demand is growing with a distressing rate as the world population increases and the irrigated agriculture expands. Water scarcity is becoming a problem in all continents with increasing demand and overused resources. Water desalination can be a sustainable solution to the water shortage concern in the world, but it is costly to build and operate large-scale desalination plants [1]. The reverse osmosis process is dominating the desalination industry [2]. There are several disadvantages of reverse osmosis process that make it undesirable such as high fouling propensity and high operating pressures [2]. Recently, membrane distillation (MD) desalination is considered as a viable option to the reverse osmosis process [3].

MD is a thermally driven separation process where only water vapor molecules can pass through a microporous hydrophobic membrane. The driving force in the MD system is the vapor pressure difference across the membrane induced by the temperature difference between the warm feed and the permeate solution. MD is gaining renewed attention as a promising method for water desalination since it operates under low temperatures (< 90 ℃) which makes it easy to use waste heat or solar energy as a heat source [4]. Another important feature of MD process is that the membrane is less prone to potential fouling so it could be a desirable option for high concentration separation applications such as the treatment of highly contaminated water [5,6]. There are various MD configurations depending on the design of the permeate channel. The Direct Contact Membrane Distillation (DCMD) has the pure liquid-phase water flows inside the permeate channel. The Vacuum Membrane Distillation (VMD) uses a vacuum pump to create a negative pressure within the permeate channel to drive the water vapor through the membrane. In

the Air Gap Membrane Distillation (AGMD), the permeate channel is divided into two subdivisions. The first segment that is adjacent to the membrane holds the stagnant air while the second segment is a cold surface. The water vapor permeating from the feed channel crosses the air gap and condensates over the cold surface. In the Sweeping Gas Membrane Distillation (SGMD) air is introduced in the permeate channel to sweep the vapor permeating through the membrane. The water vapor is then condensed outside the module in a suitable condenser.

In DCMD, the hot solution and the cold fresh water are in direct contact with the membrane surface. Evaporation takes place at the membrane pores at the feed side, vapor molecules pass through the membrane pores and condense at the permeate side over the surface of the membrane. DCMD module can be built using different membrane configurations such as flat sheets, spiral wound, and hollow fiber [7]. Beside water desalination, DCMD is used in several other applications such as chemical, textile, and pharmaceutical industries [7].

The schematic diagram of the DCMD module consisting of the feed and permeate channel separated by a hydrophobic membrane is shown in Fig. 1. The hot solution with a temperature T_f flows in the feed channel and the cold fresh water with a temperature of T_p flows in the permeate channel. For the fresh water production – the passage of the water vapor from the feed to the permeate channel - T_f must be larger than T_p so that the vapor pressure difference across the membrane between the feed and the permeate side is positive. The transfer of water vapor from the feed channel to the permeate channel creates undesirables yet inevitable phenomena named the temperature and concentration polarization. Since the driving force for the separation process is the difference in the vapor

pressure; it is affected by the change in temperature. Naturally, heat is lost from the feed channel to the permeate channel by two modes, conduction and evaporation. The heat loss by conduction is governed by Fourier law. The thermal conductivity, thickness of the membrane, and the temperature difference across the membrane are factors affecting the heat loss by conduction. The heat loss by evaporation is governed by the amount of vapor transfer from the feed to the permeate side and the enthalpy of water. The heat loss by evaporation is dominant in membrane distillation systems. The heat transfer reduces the temperature of the feed water and increases the temperature of the pure water along the membrane creating a thermal boundary layer. The second undesirable phenomenon is the concentration polarization. The feed water enters the membrane module as a contaminated stream or sea or brackish water. In the current study the feed is considered free from contaminant and has only high solute levels. As the water vapor permeates to the permeate channel, the solute starts to accumulate in the feed channel since the membrane is designed to allow the passage of water vapor molecules only. The accumulation of the solute increases along the membrane surface and this give rise to the development of a concentration boundary layer.

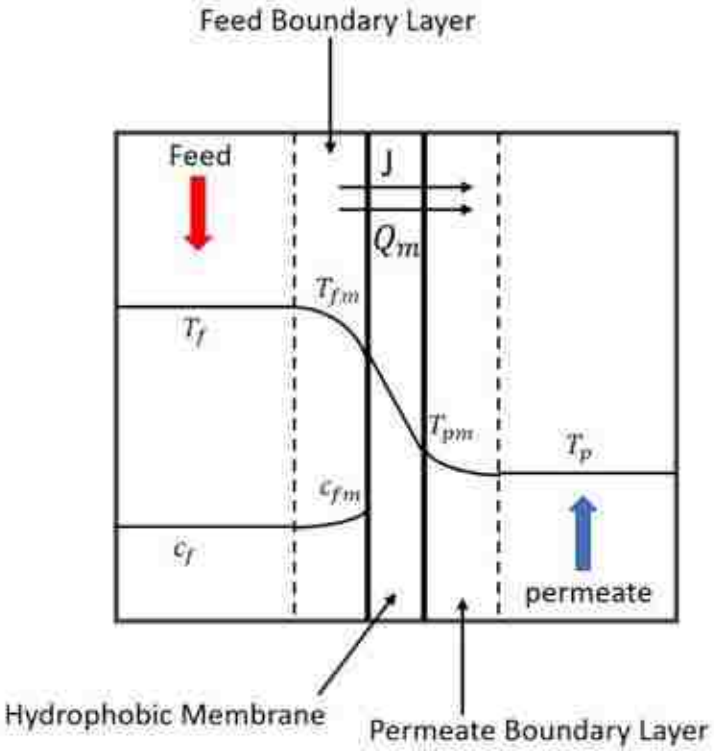

Figure 1. *Schematic diagram of the DCMD process*

Literature Review

Several researchers investigated the effect of membrane properties and operational parameters on the DCMD. Adnan et al. [8] studied the effect of membrane support layer on the flux performance by conducting experiments in a DCMD module. They reported that the water flux was reduced by 56% when the membrane support layer is present. Hayer et al. [9] conducted simulations in a two-dimensional DCMD module to determine the velocity, temperature and concentration field. They reported that the permeate flux is strongly influenced by the membrane thickness and the inlet feed temperature, but it is hardly affected by the concentration of the feed solution. Li et al. [10] examined the effect of the operating conditions on the performance of the DCMD and VMD module containing hollow fiber membranes. They documented that the permeate flux decreases in DCMD and VMD module with increasing the membrane thickness. The experimental methods provide valuable insight for DCMD systems, but it should be accompanied by CFD tools to conduct an in-depth investigation of the DCMD modules. Francis et al. [11] have measured the performance of the DCMD process for desalting seawater. The high rate of water permeation was attained for the inlet feed temperature of 80℃ and the permeate temperature of 20℃. Also, they reported that the permeate flux is not sensitive to the concentration of the feed solution. Park et al. [12] simulated the desalination process in a two-dimensional DCMD module to characterize the flow, temperature and concentration field. The effects of the operating parameters on the flux performance of the module were investigated. They concluded that the water permeation rate and the intensity of temperature polarization increases as the inlet feed temperature is increased. Soukane et al. [13] performed a computational study for water desalination process in three-dimensional

DCMD modules. Flow simulations were conducted in the feed channel, and the effect of the permeate channel was included through boundary conditions imposed on the temperature, concentration, and the velocity field. They have considered two membranes with different thickness, pore size, and porosity, and concluded that the temperature polarization effects are dominant at all inlet feed temperatures. Bouchrit et al. [14] conducted experiments to study the capability of DCMD to treat reverse osmosis brine by using a flat sheet membrane and showed that the DCMD could be used effectively in high concentration applications. Hwang et al. [15] have studied the effect of module dimensions on the DCMD flux performance using the co-current and counter-current flow modes. Their results showed that the flux obtained from two flow modes is similar, and the vapor pressure difference across the membrane decreases with the increase of the module length.

Various types of mixing promoters have been considered in DCMD systems. Phattaranawik et al. [16] studied experimentally the effect of net-type spacers on heat and mass transfer in DCMD module. Spacers with varying filament angles and voidages were tested. The results showed that the presence of spacers enhanced the water vapor flux by 60% and the heat transfer coefficient was doubled compared to an empty channel. The optimum voidage of the spacers was found to be 0.6. Cipollina et al. [17] have conducted numerical simulations on the effect of the presence of spacer in DCMD systems. Spacers with different filament diameters and angles were considered. The results show that the module with thinner spacers performs better mitigating the temperature polarization with lower pressure drop. The pressure drop reduces when the spacers are placed parallel to the flow. Yun et al. [18] experimentally investigated the effect of compactness of spacer on the performance of DCMD systems They showed that the coarsely placed spacers

performed better than fine spacers. Also, is the module containing spacers in the feed channel performs better than the module with spacers in the permeate channel. They recommended that spacers with moderate or lower flow rate should be used to promote turbulent or mixing. Manawi et al. [19] developed a theoretical model and conducted an experimental study to assess the temperature polarization in DCMD systems with high salinity feed solution. In their experimental work, spacers were used near the membrane surface. The results show that the temperature polarization increases with increasing feed temperature. The temperature polarization can be lowered by increasing the flow rate in the feed channel. Also, the presence of spacers had a positive impact on temperature polarization and enhanced the overall system performance. Chang et al. [20] conducted several CFD simulation on DCMD systems with the presence of net-type spacers with two different angles of 90° and 45° with the same filament diameter. In the simulations, pure water was used in both channels. The results indicate that the DCMD system performed better with the 45° filament angle. Also, the system performance is influenced profoundly by the flow rate in the feed channel containing spacers. Fard et al. [21] conducted a case study to examine the effect of spacers in the flow channel. The spacers used had a filament angle of 90° that was perpendicular to the flow. The resulted enhancement in the flux with the use of spacer was 51% compared to the flux of the module without spacers. Seo et al. [22] conducted a numerical study to optimize the use of spacers in DCMD systems. The authors have developed 51 spacers design. Their main results show that the symmetrical circular zigzag spacer design with a large diameter is recommended if the pumping power is not a concern for the operation. Spacers with fewer filaments of smaller diameter are recommended to minimize the pressure drop along the flow channel if the heat source is

not a concern for the operation. Katsandri [23,24] conducted a CFD study to analyze a DCMD system with a flat membrane module filled with spacers. The spacers considered in the study were of net-type spacers with the filament angle of 0°, 45°, and 90°. The results indicate that the filament angle of 45° performed better compared with the other two angles. The 45° fillament angle produced better mixing with enhanced shear stress over the membrane surface and minimum temperature polarization. Taamneh et al. [25] conducted experimental measurements and CFD simulations to study the effect of adding spacers made of intersecting filaments in DCMD module. . Various configurations of filaments are considered in their study. The results indicate that the spacer orientation influence the heat and mass transfer in the module drastically. The filaments with 45° to the flow direction perform the best. Kim et al. [26] conducted experiments and theoretical study to examine the effect of non-woven net-type spacers in DCMD systems. The thickness, filament angles, and filament count were set as variables in the study. The spacers were placed in the feed channel, permeate channel, and in both channels. The results indicated that the performance has increased by 7-19% with spacers in the permeate channel, 33% with spacers in the feed channel, and 43% with spacers in both channels compared to the flux without spacers.

Yu et al. [27] conducted a CFD study on the effect of baffles in a hollow fiber membrane module in DCMD systems. The baffles are attached to the walls of the shell in the feed side. The results indicate that the temperature polarization increases with increasing the permeability. Thus, the existence of the baffles will help in mitigating the temperature polarization. As the permeability is lowered, the attained flux is lower, and

thus no apparent temperature polarization is observed. With membranes with low permeability, baffles have negligible influence on the permeating vapor flux.

Spacers are widely used in DCMD systems to promote mixing, mitigate polarization, and enhance the flux performance. Microstructures over the membrane and channel surface could also be used to mitigate temperature and concentration polarization in membrane separation modules. Membrane corrugations have been used in reverse osmosis [28] and forward osmosis module [29] to mitigate polarization and enhance the module performance. Yang et al. [30] conducted CFD simulations in hollow-fibers DCMD systems having microstructures over the surface of membranes. Surface patterns of wavy and gear structure were considered. The results show that membranes with gear structures had a better performance than membranes with wavy structures. The flux with gear-structured hollow fibers was increased by 66% compared to that with straight hollow fibers. Mabrouk et al. [31] experimentally investigated the effect of channel corrugation in DCMD systems. They have used a lab scale model with a corrugated feed channel to enhance the mixing near the membrane wall. The results show that the flux and the thermal efficiency were enhanced by 44%, and 33%, respectively.

Hitsov et al. [32] documented an extensive review of the mathematical modeling for the membrane distillation process. They stated that even though the MD process was discovered over 50 years ago, commercialized industrial-scale MD desalination modules haven't been developed and deployed. They recommended that the MD community must have an in-depth understanding of the transport phenomena inside the channels and through the membrane. This detailed understanding could be provided by combined experimental measurements and CFD simulations utilizing accurate mathematical modeling. There were

only a few previous CFD investigations as presented and discussed above. Many of these studies have omitted some aspects of important physical phenomenon involved in MD systems by overly simplifying the model or the geometry. It is imperative to carry out more computational studies to better understand MD systems so that MD separation process can become a competitive technology.

Chapter 2: Mathematical Model

Three-dimensional steady state incompressible flows are considered in the feed and the permeate channel. The conservation of mass is written as

$$\nabla \cdot \vec{U} = 0 \tag{1}$$

The momentum equation is

$$\vec{\mathrm{U}}.\nabla\,\vec{\mathrm{U}} = \frac{1}{\rho}\left[-\nabla \mathrm{p} + \nabla.\left(\mu\nabla\vec{\mathrm{U}}\right)\right] \tag{2}$$

The equations governing the solute mass and energy transport are described by

$$\left(\vec{U}\cdot\nabla\right)\mathrm{c} = D\nabla^2 c \tag{3}$$

$$\vec{U}\,.\nabla T = \frac{k_f}{\rho c_p}\nabla^2 T \tag{4}$$

Here ρ is the density, p is the pressure, μ is the viscosity, c is the solute mass fraction, D is the solute diffusion coefficient, T is the temperature, k_f is the thermal conductivity of the solution, c_p is the specific heat of the water, and $\vec{U}$ is the velocity vector. The fluid viscosity is taken as a function of temperature and salt mass fraction

$$\mu = 0.001ln\left(-3.79418 + \frac{604.129}{139.18 + T}\right)\left(1 + A_\mu c + B_\mu c^2\right) \tag{5}$$

Eq. 5 is valid for the temperature ranging from 20 ℃ to 180 ℃ and for the salinity ranging from 0 to 130 $g\ kg^{-1}$ [33,34]. Here $A_\mu = 1.474 \times 10^{-3} + 1.5 \times 10^{-6}\,T - 3.927 \times 10^{-8}\,T^2$ and $B_\mu = 1.073 \times 10^{-5} - 8.5 \times 10^{-8}\,T + 2.23 \times 10^{-10}\,T^2$ are temperature dependent functions.

The equations (1-4) are used to simulate laminar flows in the empty module while the SST *k-ω* turbulence model equations are used to simulate flows in the module containing spacers. The SST *k-ω* turbulence momentum mass and energy equation

$$u_j \frac{\partial u_i}{\partial x_j} = -\frac{1}{\rho}\frac{\partial p}{\partial x_i} + \frac{1}{\rho}\frac{\partial}{\partial x_j}\left((\mu + \mu_t)\frac{\partial u_i}{\partial x_j}\right) \quad (6)$$

$$u_j \frac{\partial c}{\partial x_j} = \frac{\partial}{\partial x_j}\left((D + \frac{\mu_t}{\rho\, Sc_t})\frac{\partial c}{\partial x_j}\right) \quad (7)$$

$$u_j \frac{\partial T}{\partial x_j} = \frac{\partial}{\partial x_j}\left((\frac{k_f}{\rho c_p} + \frac{\mu_t}{\rho\, Pr_t})\frac{\partial T}{\partial x_j}\right) \quad (8)$$

Here, Sc_t is the turbulent Schmidt number, Pr_t is the turbulent Prandtl number. The eddy viscosity is

$$\mu_t = \rho \frac{a_1 k}{\max(a_1\omega, SF_2)}$$

The turbulent kinetic energy k and the specific dissipation rate ω are given as

$$u_i \frac{\partial(\rho k)}{\partial x_i} = \tau_{ij}\frac{\partial u_i}{\partial x_j} - \beta^*\rho\omega k + \frac{\partial}{\partial x_j}\left((\mu + \sigma_k\mu_t)\frac{\partial k}{\partial x_j}\right) \quad (9)$$

$$u_i \frac{\partial(\rho\omega)}{\partial x_i} = \frac{\gamma}{\nu_t}\tau_{ij}\frac{\partial u_i}{\partial x_j} - \beta\rho\omega^2 + \frac{\partial}{\partial x_j}\left[(\mu + \sigma_\omega\mu_t)\frac{\partial\omega}{\partial x_j}\right] + 2\rho(1 - F_1)\sigma_{\omega 2}\frac{1}{\omega}\frac{\partial k}{\partial x_j}\frac{\partial\omega}{\partial x_j} \quad (10)$$

where S is the vorticity magnitude, $\gamma, a_1, \beta, \beta^*, \sigma_k, \sigma_\omega$ and $\sigma_{\omega 2}$ are the closure coefficients, and F_1, F_2 are the blending functions. Details of the closure coefficients and blending functions can be found in [35].

The water flux (J) in the MD process is a function of the vapor pressure difference across the membrane, and it is calculated by the following equation [32].

$$J = C\left(P_{v,f} - P_{v,p}\right), \quad (11)$$

$P_{v,f}$, $P_{v,p}$ are the vapor pressure of the feed and the permeate solution at the membrane surface, respectively. They are determined as a function of local temperature and concentration using the modified Antoine equation [13]

$$P_v = \frac{\exp\left(23.1964 - \frac{3816.44}{T - 46.13}\right)}{1 + 0.57357\left(\frac{c}{1000 - c}\right)} \tag{12}$$

where c is in the unit of g/kg. C, the membrane permeability, is obtained based on the dusty gas model (DGM) [32,36,37]. The DGM describes the diffusion inside the membrane to occur by a combination of several mechanisms. These mechanisms are Knudsen diffusion, molecular diffusion and viscous diffusion. The viscous diffusion could be neglected in DCMD module since the difference in the total pressure across the membrane is small. The Knudsen number, *Kn*, determines the diffusion resistance that dominates the mass transport through the membrane

$$Kn = \lambda / d_p$$

Here the mean free path is

$$\lambda = (K_B T)/\sqrt{2}\pi \bar{P} \sigma^2$$

where d_p is the membrane pore diameter, K_B is the Boltzmann constant, T is the inlet feed temperature, $\bar{P}$ is the average pressure across the membrane pores, and σ^2 is the collision diameter of water. The Knudsen diffusion (C_K) is used to describe the membrane permeability when the mean free path of water vapor molecule is larger than the membrane pore diameter (Kn >1). In this regime, collisions of molecules with the pore wall dominate the vapor transport through the membrane. The molecular diffusion (C_m) is considered as a membrane permeability when the membrane pore diameter is much larger than the mean free path of water vapor molecule (Kn <0.01). In this regime, the trapped air within the

membrane pore adds resistance to the movement of vapor molecules, and collisions of molecules with the pore walls can be ignored. In the transition regime ($0.01 < Kn$ <1), the combined Knudsen and the molecular diffusion (C_{K+m}) are used to describe the membrane permeability. Table 1 shows three models used for determining the membrane permeability [32,37–39].

Table 1. *Permeability models*

Knudsen number	Mass transfer coefficient equation
$Kn > 1$	$C_{K=} \frac{2r\varepsilon}{3\delta\tau}\sqrt{\frac{8M_w}{\pi RT_{ave}}}$
$Kn < 0.01$	$C_m = \frac{\varepsilon}{\tau\delta}\frac{PD_v}{P_a}\frac{M_w}{RT_{ave}}$
$0.01 < Kn < 1$	$C_{K+m} = \left(\frac{3\delta\tau}{2r\varepsilon}\sqrt{\frac{\pi RT_{ave}}{8M_w}} + \frac{\tau\delta}{\varepsilon}\frac{P_a}{PD_v}\frac{RT_{ave}}{M_w}\right)^{-1}$

Here, δ is the membrane thickness, τ is the membrane tortuosity, r is the membrane pore radius, ε is the membrane porosity, R is the universal gas constant. The average temperature inside the membrane pore is

$$T_{ave} = \frac{T_{fm} + T_{pm}}{2}$$

where T_{fm} is the temperature at the feed side, T_{pm} is the temperature at the permeate side, M_w is the molecular weight of water, P_a, the partial pressure of air, is taken as the atmosphric pressure [40]. The product of the total pressure and the diffusion coffecient of vapor is [40,41]

$$PD_v = 1.895 \times 10^{-5}\, T^{2.072}$$

The total heat transfer through the membrane ($\dot{Q}_m$) includes the conduction heat transfer ($\dot{Q}_c$) and the latent heat of vaporization ($\dot{Q}_v$) [42]

$$\dot{Q}_m = \dot{Q}_c + \dot{Q}_v = \frac{k_m}{\delta}(T_{fm} - T_{pm}) + JH_v \quad (13)$$

where the enthalpy of vaporization is [13]

$$H_v = 1753.5\,T + 2024.3 \times 10^3$$

The thermal conductivity of the membrane is

$$k_m = \left(\frac{\varepsilon}{k_g} + \frac{1-\varepsilon}{k_s}\right)^{-1}$$

The thermal conductivity is a function of the membrane porosity, the thermal conductivity of vapor (k_g), and the thermal conductivity of the membrane material (k_s) [43]. In DCMD systems, it is reported that 60 to 80 % of the total heat is transferred by the vapor across the membrane [36,44].

Temperature polarization is a well-known phenomenon in the MD system. It happens as a result of the heat transfer at both sides of the membrane, as shown in Fig 1. Temperature polarization is responsible for reducing the driving force in DCMD systems. Temperature polarization coefficient (TPC) measuring the intensity of temperature polarization is defined as the ratio of the temperature difference across the membrane to the difference of bulk temperature of the feed and the permeate solution at the local cross-section

$$\text{TPC} = \left(\frac{T_{fm} - T_{pm}}{T_f - T_p}\right) \quad (14)$$

The concentration polarization is a common issue in most membrane desalination processes [28,45–47]. As the water vapor passes through the membrane, the solute accumulates on the membrane surface causing the concentration polarization. The ratio of the local concentration on the membrane surface over the inlet feed concentration defines the concentration polarization coefficient (CPC)

$$\mathrm{CPC} = \left(\frac{c_{fm}}{c_f}\right) \tag{15}$$

At the exit, the specified pressure and the zero-gradient for the temperature and concentration field are imposed in each channel. The inlet boundary conditions are

$$u = U_{f,ave},\ v = 0,\ w = 0,\ T = T_{f,in},\ c = c_{f,in} \quad \text{for the feed stream} \tag{16}$$

$$u = U_{p,ave},\ v = 0,\ w = 0,\ T = T_{p,in},\ c = 0 \quad \text{for the permeate stream} \tag{17}$$

The membrane is treated as a functional surface where the water flux couples with the local feed and permeate temperature and the feed concentration. With the suction rate calculated by $V_m = J/\rho$ the membrane boundary conditions imposed on the surface of the membrane are

$$u = 0,\ v = V_m,\ w = 0,\ k_c \frac{\partial T}{\partial y} = -\dot{Q}_m, \text{ and } D \frac{\partial c}{\partial y} = V_m c \quad \text{at the feed side} \tag{18}$$

$$u = 0,\ v = -V_m,\ w = 0,\ k_c \frac{\partial T}{\partial y} = \dot{Q}_m, \text{ and } \frac{\partial c}{\partial y} = 0 \quad \text{at the permeate side} \tag{19}$$

The boundary conditions imposed on the feed and the permeate channel walls are

$$u = 0,\ v = 0,\ w = 0,\ \frac{\partial T}{\partial y} = 0, \text{ and } \frac{\partial c}{\partial y} = 0 \tag{20}$$

Chapter 3: A Parametric Study - Effect of Membrane Properties and Operational Parameters

Computational fluid dynamics simulations were conducted to investigate the effects of the membrane properties and operational parameters on the system performance in three-dimensional direct contact membrane distillation modules. The laminar model was employed to characterize the velocity, temperature and concentration field. The membrane thickness, porosity, pore size, feed flow rate, and the inlet feed temperature were considered in the parametric study. The water flux, the temperature and concentration polarization characteristics of the membrane were determined. The permeation flux and the intensity of temperature and concentration polarization increase as the thickness is reduced and the porosity and the pore size are increased. The rate of permeation and the polarizations are increased with an increase in flow rate.

Numerical Model, Convergence, and Validation

The module in this work is containing rectangular-shaped feed and permeate flow channels separated by an active PTFE flat sheet membrane with the dimensions of each channel $50h$ in length and $5h$ in width where h is the height of the channel. Reynolds number for flows in each channel is defined based on the averaged flow velocity U_{ave} at the inlet and the channel haydrulic daimeter h_d for each stream

$$Re = \frac{U_{ave}\rho h_d}{\mu}$$

Here ρ is the density and μ is the dynamic viscosity of each streaming fluids. The inlet concentration of the feed solution, $0.035\ \mathrm{kg_{solute}}/\mathrm{kg_{water}}$, represents seawater

desalination. In the permeate channel, the inlet temperature and *Re* are fixed at 20 ℃ and 330 for all simulations. Fluent 17.1 was utilized to conduct simulations in three-dimensional DCMD module. The geometry of the module was created using Solidworks and imported to the Ansys meshing tool for discretization. The membrane is treated as a functional surface where the suction rate, local temperature and concentration are coupled. The boundary conditions imposed at the surface of the membrane were executed using a user-defined function (UDF). The variation of the membrane permeability and the viscosity was also executed using a UDF. The density, specific heat, and the thermal conductivity of the feed and permeate solution were assumed constant [48]. The solute diffusion coefficient was considered constant [13]. The SIMPLE algorithm was used for the pressure-velocity coupling. The second order upwind algorithm was used for the momentum, energy, and the user-defined scalar (solute transport).

A structured mesh is used to discretize the domain. Inflation layer is employed near the membrane surface on both sides of the channel to resolve the velocity, temperature and the concentration field inside the boundary layer. It was previously shown that a first layer thickness of $5\ \mu m$ is resonable for capturing the concentration polarization [49]. The present simulations reveal that $\pm 3\ \mu m$ variations in the first layer thickness had negligible influence on the prediction of the membrane performance.The mesh density of *N1* = 1 million elements, *N2* = 1.6 million elements, *N3* = 3.2 million elements, and *N4* = 6.4 million elements are selected to conduct the mesh independence test in the empty module for *Re* = 1,500 in the feed and *Re* = 330 in the permeate channel. Fig. 2a shows the normalized stream-wise velocity at x/*h* = 25 and z/*h* = 2.5. The velocity profiles obtained by the mesh density of *N1*, *N2*, *N3*, and *N4* are nearly the same. Figs. 2b and 2c show the

normalized concentration and temperature along the membrane surface at z/h = 2.5 from the inlet to the outlet. The temperature profiles at each side of the membrane predicted using *N1*, *N2*, *N3*, *N4* are nearly identical. The concentration profiles at the feeed side obtained by *N1* and *N2* display slight deviations while the concentration profiles obtained using *N3* and *N4* are nearly the same. It is concluded from the mesh optimization study that a mesh density of 3.2 million ensures spatial convergence for laminar flow simulation in the emtpy module. The spatial convergence of turbulent model simulations will be discussed below along with the validation study.

The mathematical model is validated using the experimental work by Termpiyakul et al. [50] conducted in DCMD membrane systems. In the experiment, the operational parameters used were: the concentrated feed solution $35\ g/kg$, the inlet feed temperature 60 ℃, the inlet permeate temperature 20 ℃, *Re* = 8,808 for the permeate channel flow, and 9,900 ≤ *Re* ≤ 19,800 for the feed channel flow. These flow rates in each channel correspond to turbulent channel flows, so the validation test in the DCMD module were conducted using the $k-\omega$ Shear Stress Transport model. The membrane properties for the validation study are taken from the experiments: the permeability of the PVDF membrane $6.67\ \times\ 10^{-7}\ kg/m^2\ s\ Pa$, the thermal conductivity $0.041\ W/m\ K$, and the thickness $126\ \mu m$. The permeate flux predicted agrees well with that measured for various values of the feed channel Re, as listed in Table 2. It is demonstrated that the mathematical models characterizing the transport phonemona in both channels and through the membrane are validated. The mesh density of 10.5 million elements with the maximum y+ value of about 0.3 is used in the validation study. The predictions for the validation simulations obtained using 6 million and 10.5 million mesh are nearly the same.

Table 2. *The permeation flux predicted and measured for various values of the feed channel Re*

Re	The permeation flux ($kg/m^2\,h$)		
	Experiment	Simulation	Deviation %
9,900	30.80	32.50	5.50
14,861	37.80	36.50	3.60
19,780	39.00	37.40	4.30

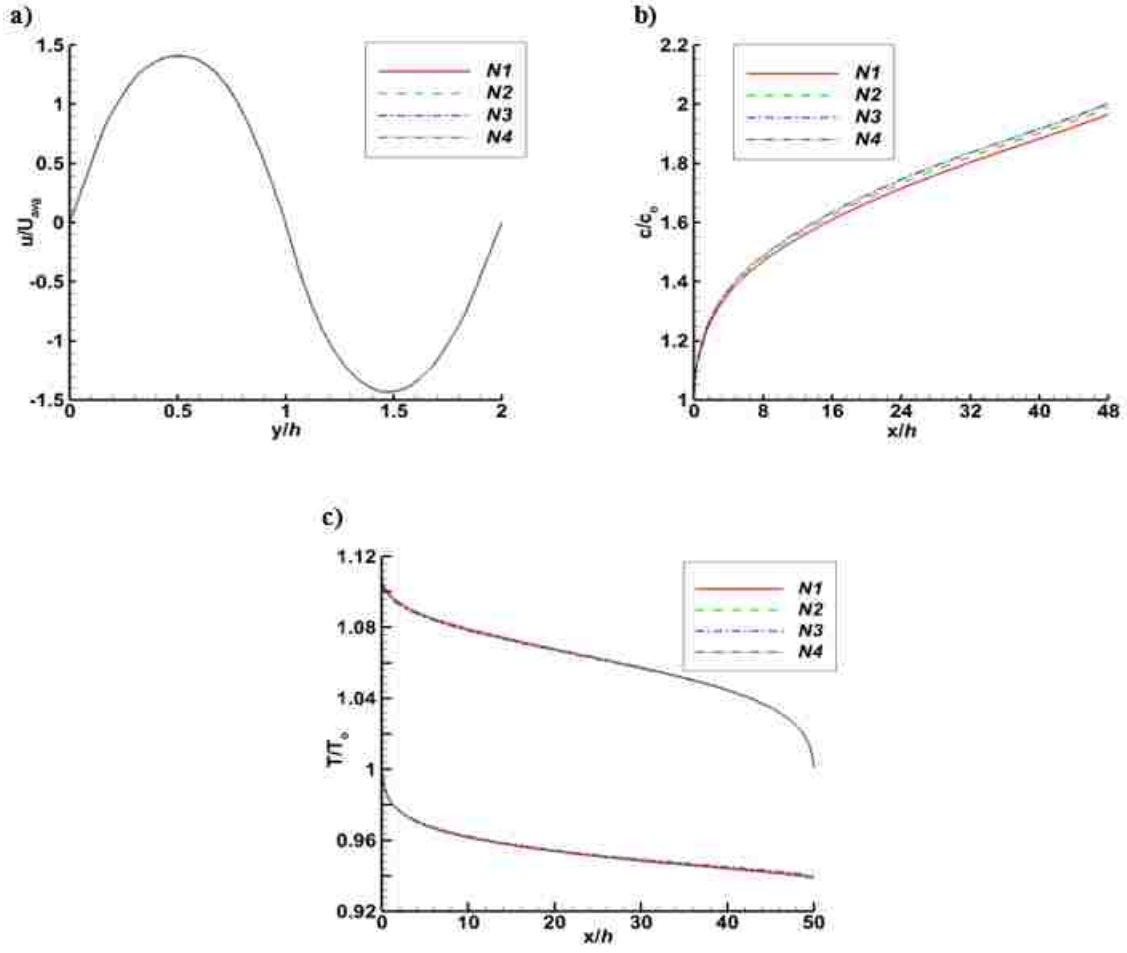

Figure 2. *Profiles of a) the stream-wise component of the velocity at z/h = 2.5 and x/h = 25, b) the normalized concentration over the surface of the membrane in the feed side at z/h = 2.5, and c) the normalized temperature over the surface of the membrane in the feed and permeate side at z/h = 2.5. The profiles are acquired using the mesh density of N1 = 1 million, N2 = 1.6 million, N3 = 3.2 million, and N4 = 6.4 million elements.*

Results

The results of the parametric study evaluating the effects of the membrane properties and the system operating parameters on the separation system performance are presented. The permeability has a profound influence on the MD system performance. Membranes of the type Hydrophobic Polyvinylidene Fluoride (PVDF) suffers from low values of permeability (ranging from 3.00×10^{-7} to 7.00×10^{-7} $kg/m^2\,Pa\,s$). Recently, researchers developed polytetrafluoroethyene (PTFE) membranes which posses higher permeablity than PVDF membranes. PTFE membranes have a permeability in the range of (6.00×10^{-7} to 2.40×10^{-6} $kg/m^2\,Pa\,s$) [42]. The membrane thickness, porosity, and pore size are other properties that could have a strong influence on the system performance. For typical MD membranes, the thickness ranges from $30\,\mu m$ to $180\,\mu m$, the porosity ranges from 0.6 to 0.88, and the average pore size ranges from $0.2\,\mu m$ to $1\,\mu m$. Table 3 shows a list of the properties of the active layer membrane used in the parametric study. The selected range of parameters is motivated by the existing commercial membranes [37].

Table 3. *Membrane parameters used in the simulations*

Parameter	**Values**
Membrane thickness, δ	100, 130, and 170 [μm]
Membrane porosity, ε	0.6, 0.7, and 0.8 [$-$]
Membrane pore size, d_p	0.20, 0.45, and 1.0 [μm]

Fig. 3 shows the average water flux as a function of the thickness for values of the porosity 0.6, 0.7, and 0.8 and the pore size 0.2, 0.45, and $1\mu m$. For the values of the pore size considered the Knudsen number is calculated to be in the range of 0.01 and 1, as listed in Table 4. The permeate flux through the membrane should be determined from the Knudsen and molecular diffusion combined, and the permeability coefficient is calculated using the relation presented in Table 1. For $d_p = 0.2\,\mu m$, the highest water flux is attained with the membrane possessing the highest porosity and the lowest thickness while the

lowest flux is attained with the membrane possessing the lowest porosity and the highest thickness, as depicted in Fig. 3a. For the same membrane thickness, the permeate flux increases as the porosity increases, and for the same porosity, the water flux decreases as the thickness increases. The similar trend is observed for $d_p = 0.45$ and $1\ \mu m$, as depicted in Fig 3b and 3c. For $d_p = 0.45\ \mu m$ the water flux level is slightly elevated for all values of the thickness and the porosity as compared to that for $d_p = 0.2\ \mu m$, even though, the pore size is increased by 125%. Similarly, with an 122% increase in the pore size between $d_p = 1\ \mu m$ and $d_p = 0.45\ \mu m$, the minuscule increase is observed in the permeated water flux, see Fig. 3b and 3c. The weak dependence of the flux on the pore size can be attributed to the fact that the membrane considered here permit flux by the Knudsen and the molecular diffusion. The resistance to the Knudsen diffusion is inversely proportional to the pore radius while the resistance to the molecular diffusion is independent of the pore size. The total resistance of the membrane to the mass diffusion is determined using the parallel circuit of the Knudsen and the molecular diffusion resistors, as presented in Table 1. Hence, the change of the pore radius does not pose a strong influence on the total membrane resistance. On the contrary, the effect of the pore size on the permeated flux is very strong for the vacuum membrane distillation (VMD) process since the total resistance of VMD membrane is determined by the Knudsen and viscous diffusion resistors connected in parallel and both resistances are a strong function of the pore size. On the other hand, the membrane thickness has a stronger influence on the water flux in the DCMD module compared to that in the VMD module. Such an in-depth comparison between the DCMD and VMD module was made possible from the results of the parametric study conducted by Usta et al. [51] for the VMD process. The increase in the pore size will make the MD

membranes susceptible to wetting as the liquid entry pressure decreases with the increased pore size. The pore size $d_p \leq 0.5\ \mu m$ is recommended for the DCMD module [52–54].

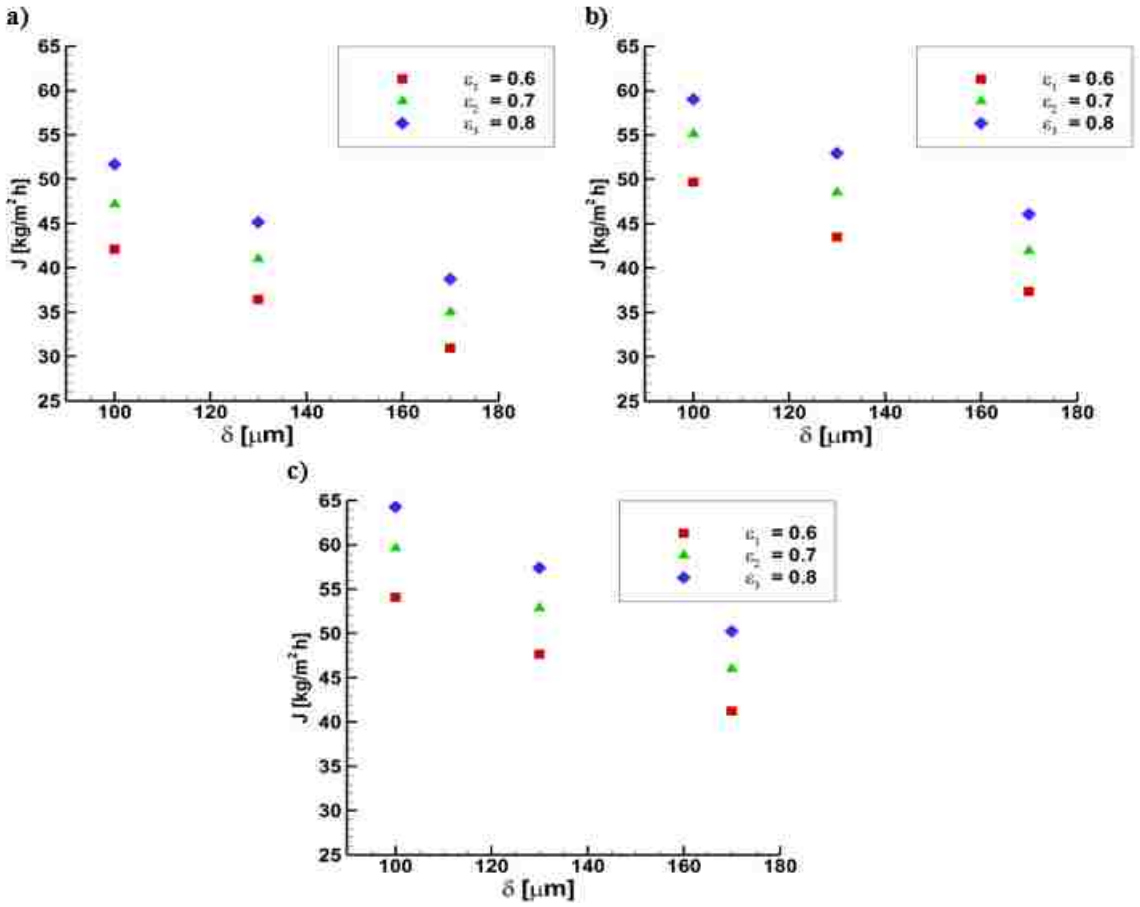

Figure 3. *The area-averaged water flux for various values of the membrane thickness and the porosity of a) pore size = 0.20 μm, b) pore size = 0.45 μm, and c) pore size = 1 μm.*

Table 4. *Knudsen number values for the selected pore sizes*

Pore Size [μm]	Knudsen Number [-]
0.20	0.78
0.45	0.35
1.00	0.16

Fig. 4 shows the average temperature polarization coefficient in DCMD systems. Ideally, the TPC should have the value of unity when there is no temperature polarization - the temperature over the membrane surface at each side would be equal to the temperature of the bulk stream in each channel. However, since there is heat removed (vaporization)

from the feed solution and gained (condensation) by the cold stream over the surface of the membrane the thermal boundary layer forms at each side and the temperature polarization occurs naturally as a result. The temperature polarization has an undesirable influence on MD performance, and it needs to be mitigated. Moreover, unlike other membrane distillation systems, there could be significant conductive heat losses across the DCMD membranes which also hinder the system performance. Fig. 4 shows the TPC for various values of the pore size and membrane thickness and porosity. There is a direct relationship with the intensity of the temperature polarization and the level of permeate flux through the membrane – the intensity of temperature polarization increases as the water flux increases. As the water permeation increases, TPC becomes smaller, as shown in Fig 3 and Fig 4. The value of TPC being further away from the unity represents the occurrence of more intense temperature polarization in the module. The heat removed from the feed solution increases linearly with the increase in the permeate flux; causing a steeper temperature gradient across the thermal boundary layer attached to each side of the membrane. Fig. 4 shows that TPC varies from about 0.67 to nearly 0.43, indicating a serious level of temperature polarization occurs in the system.

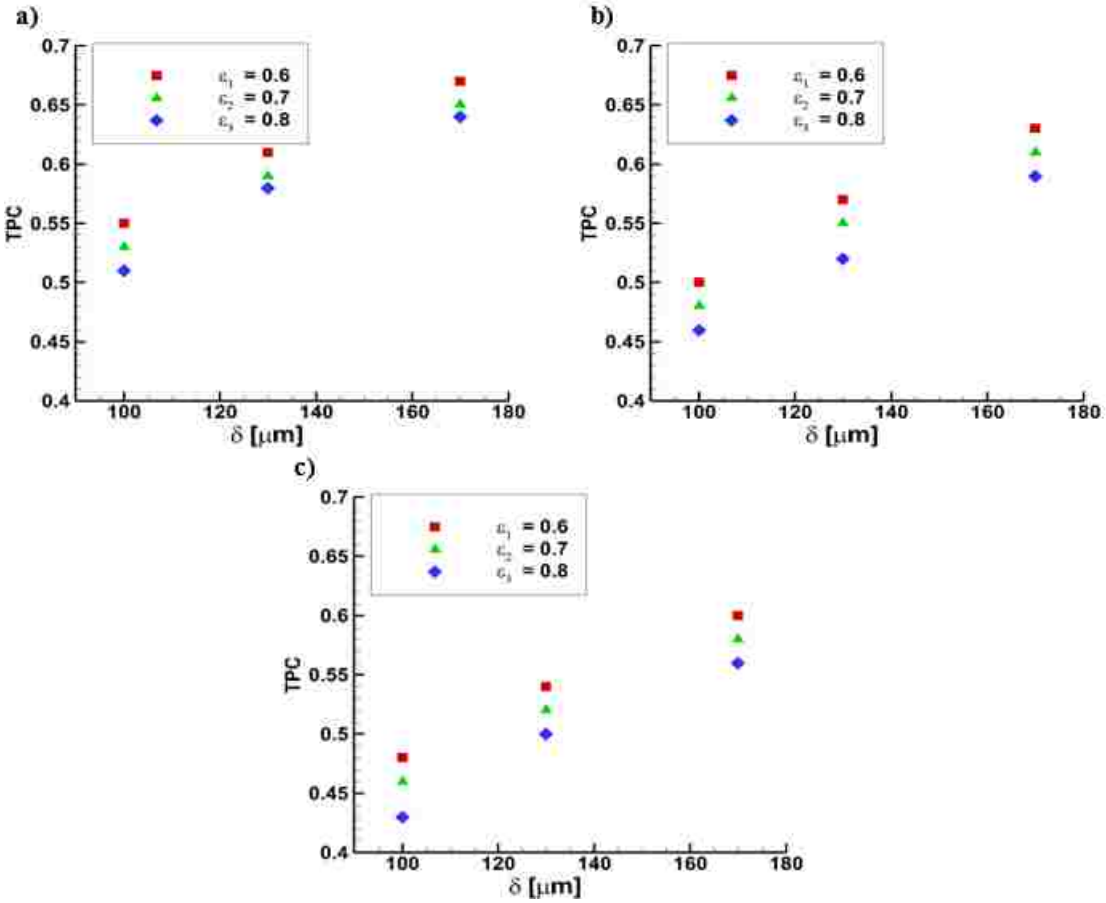

Figure 4. *The area-averaged temperature polarization coefficient for various values of the membrane thickness and the porosity of a) pore size = 0.20 μm, b) pore size = 0.45 μm,and c) pore size = 1 μm*

The concentration polarization is another critical factor determining system separation performance. Fig. 5 shows the average concentration polarization over the membrane surface in the feed channel. It is preferred for the concentration polarization coefficient to be near unity. Similarly, the concentration polarization is inevitable as the water permeates from the feed channel to the permeate channel the solute concentration near the membrane increases and the concentration boundary layer is formed. Similar to the temperature polarization, the concentration polarization is directly correlated with the magnitude of the water flux – the intensity of concentration polarization increases as the rate of permeated water is increased, as depicted in Fig. 5 and Fig. 3. Fig. 5 shows that the value of the

concentration polarization coefficient as high as about 1.7 and as low as about 1.25 is observed as the membrane properties are varied. The concentration polarization has an adverse effect over the membrane system as it reduces the water flux. It is also important to mention that the membrane fouling occurs for the continuous operation of membrane separation. The regions where fouling would occur are strongly correlated to the high concentration polarization regions over the membrane surface [45]. The remedies alleviating the concentration polarization should be considered in the design of these modules.

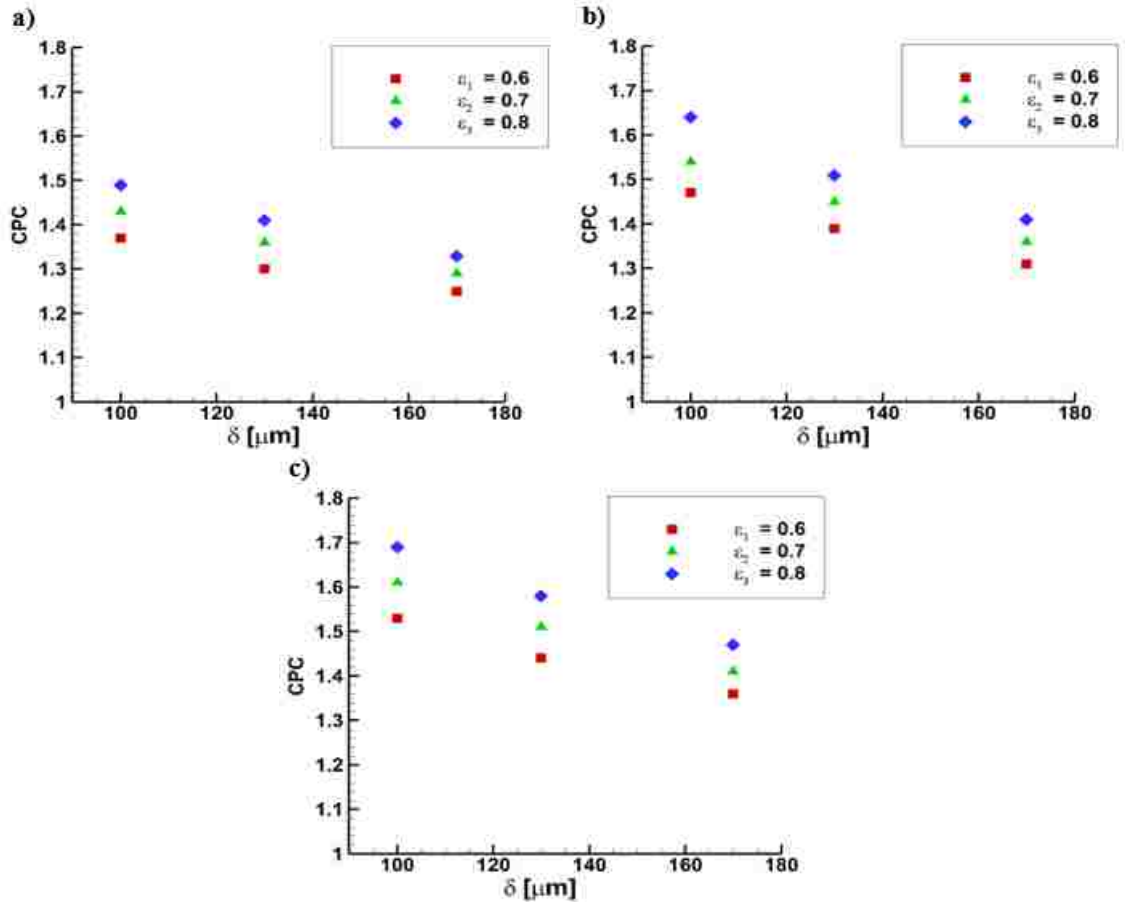

Figure 5. *The area-averaged concentration polarization coefficient for various values of the membrane thickness and the porosity of a) pore size = 0.20 μm, b) pore size = 0.45 μm, and c) pore size = 1 μm.*

It was deduced that the membrane with the thickness 100 μm, the pore size 0.45 μm, and the porosity $\varepsilon_3 = 0.80$ yield good flux performance. The effects of the operating parameters on the flux performance and the polarization are examined next. It was shown in the previous study [55] that the operating parameters of the permeate channel have a weak influence on the system performance. The permeate inlet temperature ranges between 5 to 25 ℃ in typical applications and the vapor pressure changes slightly for this range of temperature. In this work, the operating parameters controlling conditions in the feed channel are considered in the parametric study. The inlet temperature and *Re* in the permeate channel are fixed at 20 ℃ and 330 while the inlet temperature and *Re* in the feed

channel are varied. The inlet concentration of the feed solution is taken as $35\ g/kg$, which corresponds to the sea water desalination. Table 5 list the range of the feed inlet temperature and the flow rate considered in the simulations.

Table 5. *Feed operating parameters used in the simulations*

Fixed Parameters	*Re* = 1500				$T = 80$ ℃			
Variable Parameters	***T*** [℃]				**Re**			
	50	60	70	80	100	500	1,000	1,500

Fig. 6 shows the average water flux, the coefficients of the temperature and the concentration polarization as a function of the inlet feed temperature at *Re* = 1500. The vapor pressure in the feed channel increases exponentially with increasing the feed temperature as predicted by the Antoine equations (Eqn. 12). The water flux increases from $18.5\ kg/m^2h$ at 50 ℃ to $59.05\ kg/m^2h$ at 80 ℃, as shown in Fig. 6a. The effects of the local concentration at the membrane surface are included in the flux model employed in the present study even though most researchers ignore such effects [56]. Furthermore, the flux equation couples both feed and permeate temperatures along with the feed concentration to accurately predicts the variation of the water flux along the membrane surface. The TPC reduces and CPC increases as the inlet feed temperature is increased, as depicted in Fig. 6b and 6c. The heat absorbed from the feed solution by vaporization and the heat released to the cold stream by condensation increase as the rate of water permeate increases. There is another reason for the decrease of TPC: the heat loss by the conduction through the membrane. The average concentration polarization can be estimated from the water flux information by using the exponential relation given as $exp\left(\frac{J}{D\,\rho}\right)$ where *D* is the diffusivity and ρ is feed density. The fouling induced by the concentration polarization would add extra resistance to the transfer of water vapor through the membrane and will reduce the life span of the membrane [28,45,47]. It is deduced from results that the use of

mixing promoters is desired especially during operations with the higher inlet feed temperature due to the occurrence of more intense concentration and temperature polarization at these conditions. Mixing feed solution will mitigate both concentration and temperature polarization.

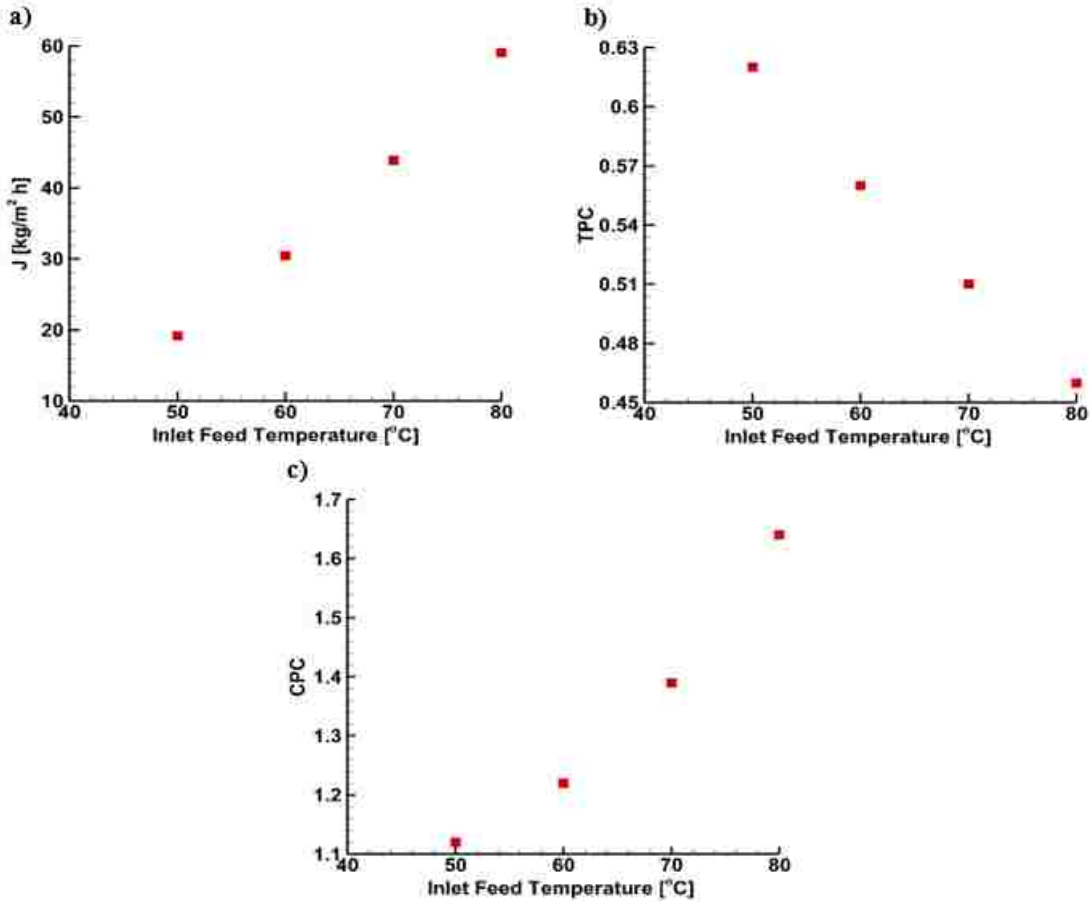

Figure 6. *The area-averaged a) water flux, b) temperature polarization coefficient, c) concentration polarization coefficient as a function of the inlet feed temperature.*

Fig. 7 shows the average water flux, the coefficients of the temperature and the concentration as a function of the flow rate at the inlet feed temperature of 80 ℃. The water flux increases as the feed flow rate increases, as shown in Fig 7a. The rate of water permeation is increased from nearly 32.31 kg/m^2h at *Re* = 100 to about 59.05 kg/m^2h at *Re* = 1500. The increase with *Re* is abrupt at lower flow rates but becomes gentler at

higher flow rates; a nearly asymptotic value is reached as the flow rate is increased. The improvement in the water flux is limited by the nature of the laminar flow. If the flow regime becomes turbulent, the improvement in the water flux could be amplified since the turbulent flows induce more mixing in both channels. The intensity of the temperature polarization improves slightly as the flow rate is increased – TPC is increased from about 0.39 to about 0.46 as *Re* is increased from 100 to 1500, as shown in Fig. 7b. At *Re* = 100, the thermal boundary layer is thick at the feed side; causing a drop in the value of the TPC. The thermal boundary layer becomes thinner as the flow rate is increased and the value of TPC increases. Within the laminar flow regime, TPC tends to the asymptotic value as *Re* is increased. The effect of the flow rate on the concentration polarization is stronger, see Fig 7c. The enhanced momentum mixing in the feed channel with increasing flow rate aids in reducing the intensity of concentration polarization. At *Re* = 100 CPC is about 2.4, and it diminishes to about 1.65 for *Re* = 1500. In DCMD modules, the influence of the concentration polarization on the membrane flux performance is not overwhelming as in other separation modules such as reverse osmosis and forward osmosis. Boubakri et al. [57] conducted experiments to compare the water flux with the pure water in the feed channel and with the highly concentrated feed water. The difference between the water flux obtained with a feed concentration of $40\ g/kg$ and with the pure water was 1.5%. This reduction does not account for the effect of fouling over the membrane. Fouling will reduce the water flux and cause membrane degradation over a longer period of operation [58]. Hence, it is still vital to mitigate concentration polarization to reduce the chance of fouling over the membrane surface [2]. A similar finding concerning the effect of feed concentration on the water flux output was reported by Al-Mutaz et al. [59].

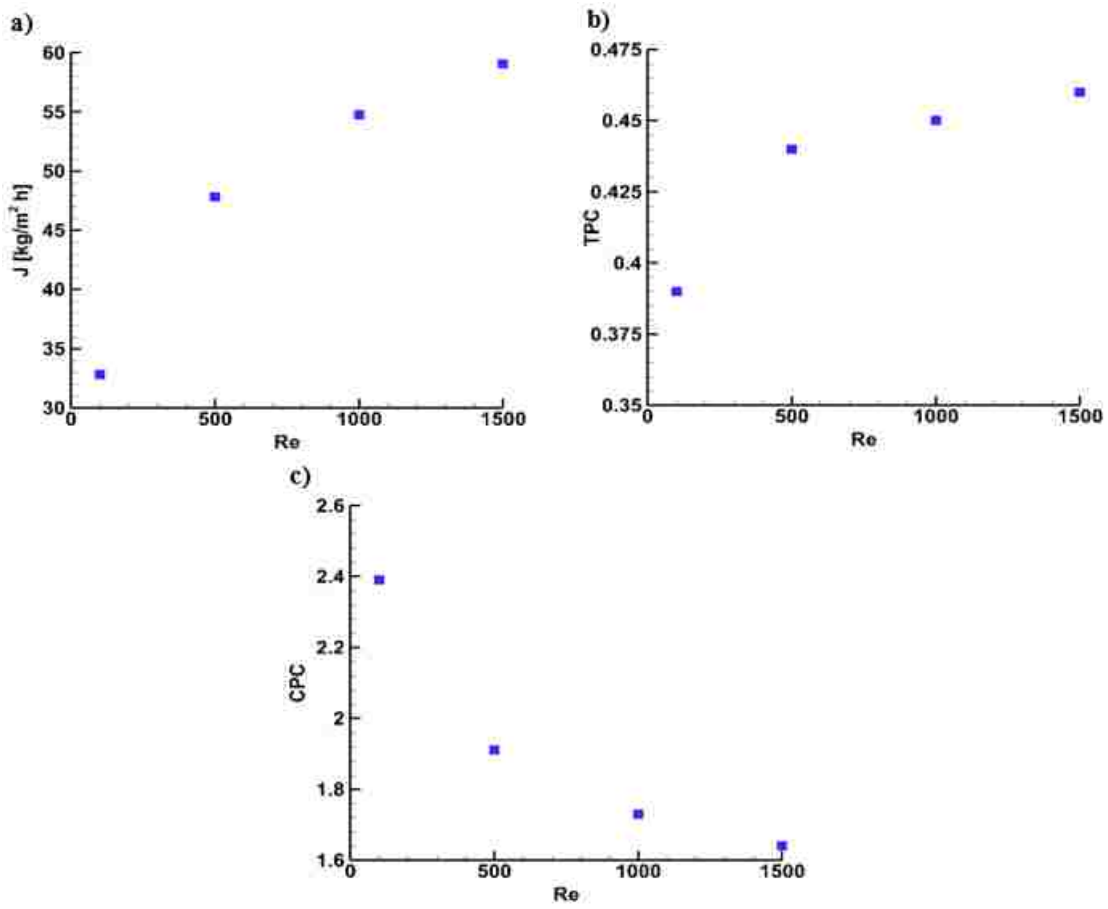

Figure 7. *The area-averaged a) water flux, b) temperature polarization coefficient, c) concentration polarization coefficient as a function of the feed flow rate*

Conclusion

Computational fluid dynamics simulations were conducted to study the flux performance, temperature and concentration polarization characteristics of the DCMD module performing the seawater desalination process. A parametric study was performed to access the influence of the membrane properties and operating parameters on the system performance within an empty module utilizing laminar flow simulations. The permeate flux increases as the thickness is decreased and the porosity and the pore size are increased. The pore size has a lesser influence compare to the membrane thickness and porosity. The

water flux and the intensity of temperature and concentration polarization are much greater at the higher inlet temperature of the feed solution. The increased feed flow rate improves the temperature and concentration polarization, but the polarization mitigation is limited when flow regime in channels is laminar

Chapter 4: The Performance Characteristics of DCMD Module Containing Spacers in Channels

This work aims to study the effects of the net-type spacers on the performance of direct contact membrane distillation (DCMD) modules. Laminar and $k-\omega\ SST$ turbulence models are used to conduct simulations in three-dimensional modules with and without spacers. The spacers are placed in the middle of the feed and permeate channel. The net type spacers of diameter $0.25h$ and $0.5h$ were considered, where h is the height of each channel. The inlet temperature of the feed and the permeate channel set to $353\ K$ and $293\ K$. The feed Reynolds number is varied (500, 1500) while the permeate Reynolds number is fixed at 330. We revealed that the presence of spacer in the flow channels mitigates both the temperature and the concentration polarization and yields higher vapor permeation. We also showed that the module containing larger size spacers yields better flux performance and lower level of temperature and concentration polarization. Moreover, the modules containing spacers become more efficient as the feed flow rate is increased.

Numerical Model and Convergence

The DCMD module consists of the feed and the permeate channel separated by the membrane. The membrane is taken to be a functional surface. The flow is not resolved within the membrane. Net-type spacers of angle $45°$ are placed in the middle of the feed and permeate channel to create mixing. The spacers are placed away from both the inlet and the outlet of the channels. The spacer diameter d_s of $0.25h$ and $0.5h$ is considered, where h is the height of either the feed or the permeate channel. The details of the geometry are shown in Fig. 8. Table 6 shows a complete list of all the membrane properties and the

operational parameters used in the simulations. The Knudsen number is calculated based on the membrane pore diameter. The Knudsen number is estimated to be 0.35. Therefore, a combination of the Knudsen and the molecular diffusion was taken in the calculation of the membrane permeability. The inlet concentration of the feed water is taken as a typical concentration of sea water. The flow rate in the feed channel was varied twice with Re_f of 500 and 1500 while keeping the flow rate in the permeate channel constant. The Reynolds number was calculated as

$$Re = U_{ave}\, \rho\, d_h/\mu$$

where d_h is the hydraulic diameter of the feed and the permeate channel.

Table 6. *Membrane properties and operating parameters*

Parameter	Value
Thickness, δ	100 [μm]
Pore size, d_p	0.45 [μm]
Porosity, ε	0.8 [−]
Tortuosity, τ	1.3 [−]
Membrane thermal conductivity, k_m	0.028 [W/m K]
Knudsen number, Kn	0.35 [−]
Feed temperature, T_f	353 [K]
Permeate temperature, T_p	293 [K]
Feed concentration, c_f	0.035 [$\mathrm{kg_{solute}}$ /$\mathrm{kg_{water}}$]
Feed Reynolds number, Re_f	500 − 1500 [−]
Permeate Reynolds number, Re_p	330 [−]

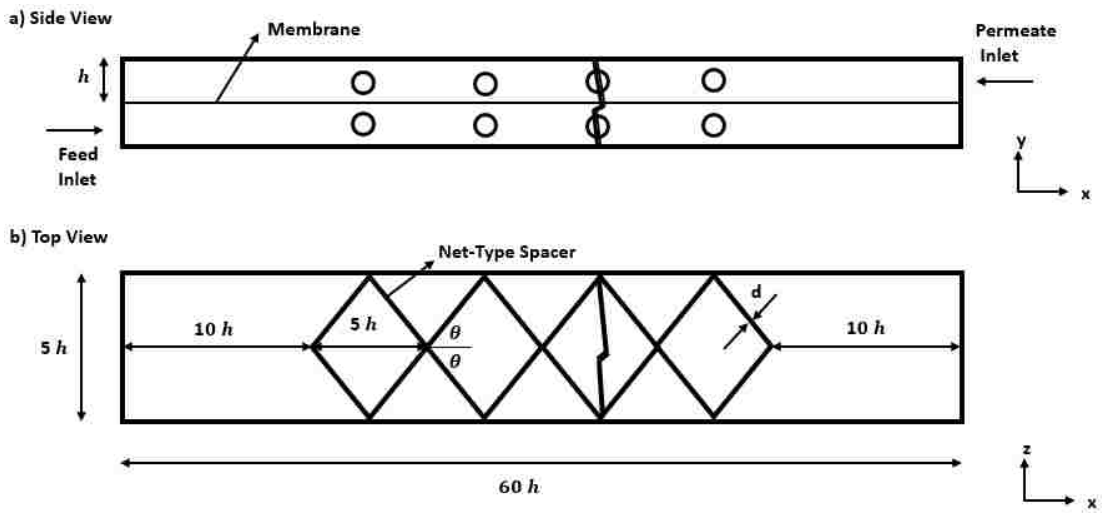

Figure 8. *Schematics of the module containing net-type spacers and dimensions of the geometry.*

In the current simulations, we employ a structured mesh for channels without spacers and an unstructured mesh for channels with spacers. The mesh near the membrane surface was refined substantially to capture the temperature and the concentration polarization accurately. The first layer thickness of the mesh near the membrane surface was taken to be 5 μm. The convergence study was carried out in the module containing spacers of diameter 0.5h for the feed Reynolds number Re_f = 1500 using mesh density of *M1* = 10 million, *M2* = 20 million, *M3* = 30 million, and *M4* = 40 million elements. The normalized stream-wise velocity of the feed solution, the normalized concentration over the membrane surface at the feed side, and the normalized temperature over the membrane surface at the feed and permeate side are plotted in Fig. 9. The profiles are determined using *M1*, *M2 M3* and *M4* mesh. The velocity profiles are acquired in the feed channel at *y/h = 0.9*. The velocity, concentration and temperature profiles obtained by *M1* and *M2* differ slightly compared to those obtained by *M3* and *M4* while the profiles obtained by *M3* and *M4* are nearly the same. The mesh density *M3* is sufficient to satisfy the mesh independence, and results presented are obtained using *M3*. Fig. 10 shows a cross section of the mesh used in

the simulations showing the refinement near the membrane surface and along the net-type spacers.

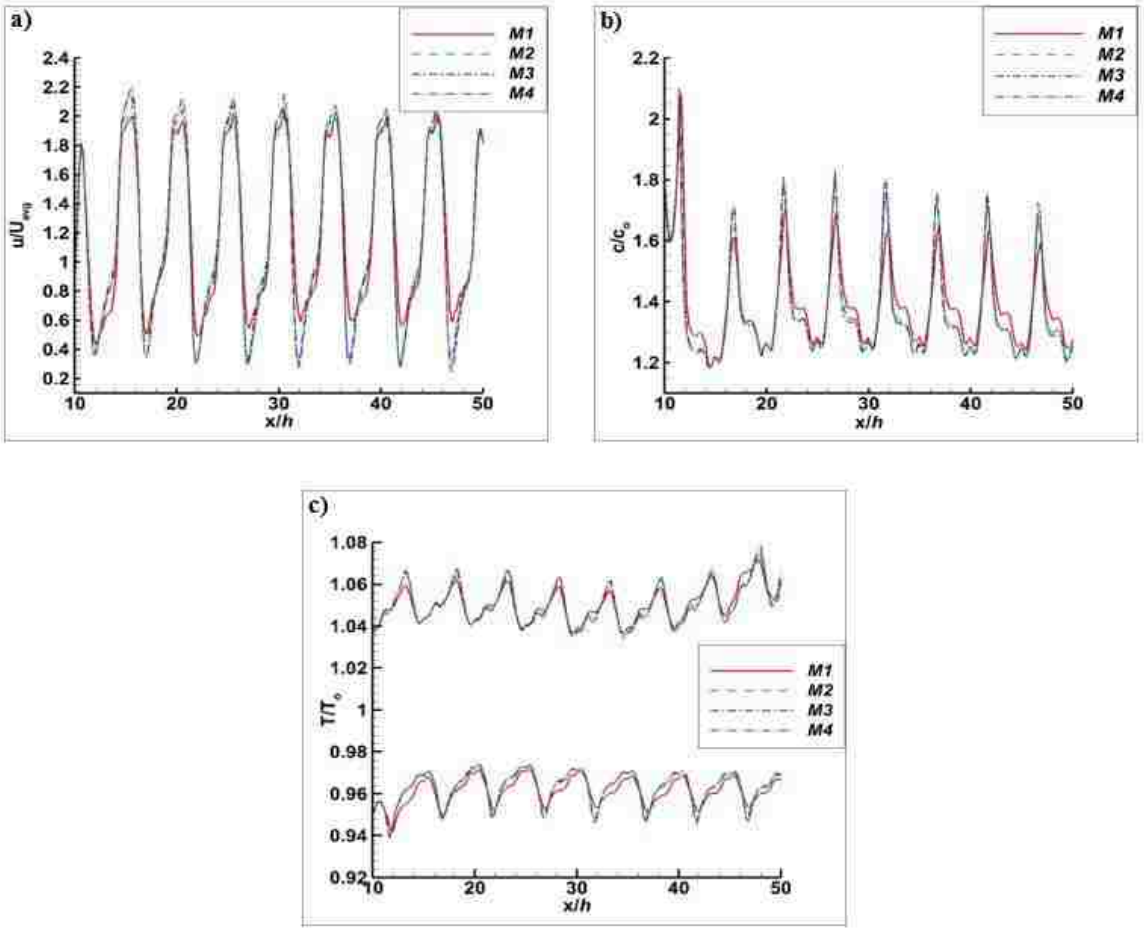

Figure 9. Profiles of a) the stream-wise component of the feed velocity at z/h = 2 and y/h = 0.9, b) the normalized concentration over the surface of the membrane at the feed side at z/h = 2, and c) the normalized temperature over the surface of the membrane at the feed and the permeate sides at z/h = 2. The profiles are acquired using the mesh density of M1, M2, M3, and M4.

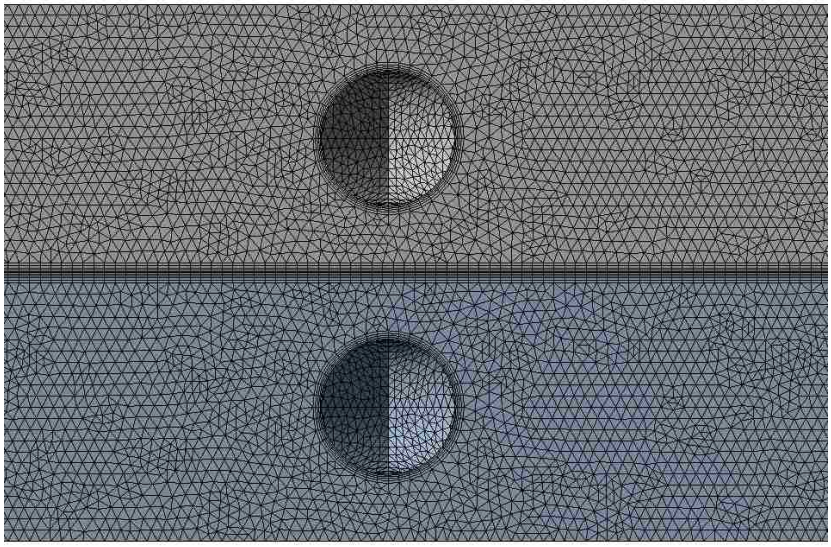

Figure 10.*A sample of the unstructured mesh for the geometry with net-type spacers.*

Results and Discussion

In this work, flow images presented are rendered between x/h = 23 and x/h = 47 in the feed channel, and between x/h = 15 and x/h = 35 in the permeate channel. The Reynolds number for the feed channel is varied while the Reynolds number in the permeate channel is kept at a constant value of Re_p = 330.

Fig. 11 shows the contours of the normalized stream-wise velocity in the feed channel for the feed Reynolds number of 500 and 1500 and the spacer strand diameter of 0.25h and 0.5h. The velocity is normalized by the average inlet feed velocity. The contours are taken at the plane of y/h = 0.9. The plane is directly below the surface of the membrane and above the spacers. The repeated flow structure induced by the spacers is seen in the stream-wise direction; indicating that the flow field is developed. The membrane flux performance, temperature and concentration polarization characteristics are determined by examining the mass, momentum and heat transport in the developed region, and thus the dependence of performance on the module length is eliminated. The low level of mixing is achieved

with small diameter spacers (d_s = 0.25h) at both flow rates, as seen in Fig. 11(a,c). The higher flow rate (Re_f = 1500) increases the mixing incrementally. In the feed channel containing spacers with a larger diameter, d_s = 0.5h, high velocity regions are observed at both flow rate. The high-speed regions become larger as the flow rate is increased. The spacer diameter should be large enough to promote proper mixing in the feed and permeate channels.

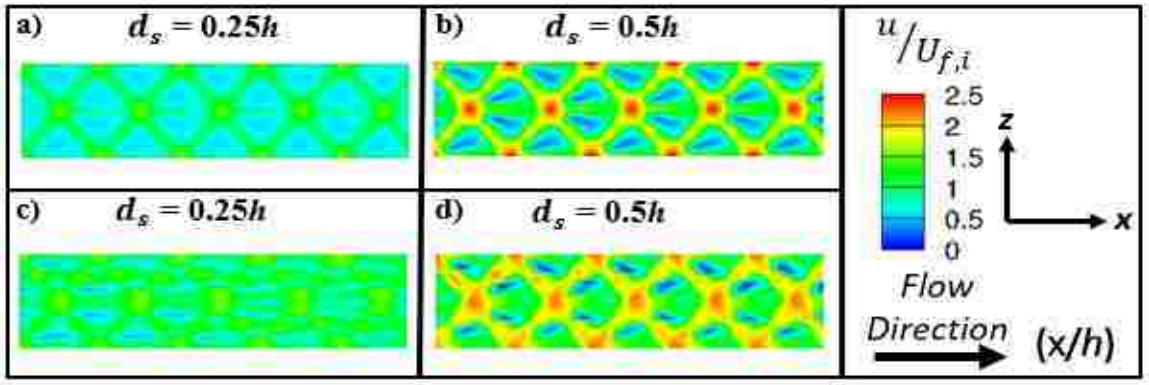

Figure 11. Contours of the normalized stream-wise feed velocity at y/h = 0.9 for a) Re_f = 500 and d_s = 0.25h, b) Re_f = 500 and d_s = 0.5h, c) Re_f = 1500 and d_s = 0.25h, d) Re_f = 1500 and d_s = 0.5h Images are rendered at 23 ≤ x/h ≤ 47.

Fig. 12 shows the contours of the normalized temperature over the surface of the membrane at both the feed and the permeate sides. The contours are normalized with the inlet temperature of each respective channel. The high mixing in the flow created by the presence of the spacers reduces the level of the temperature polarization. Ideally, the normalized temperature over the membrane surface at each side should be unity [36] to avoid a temperature polarization. Fig. 12(a) and 12(e) show the variation of the temperature over the membrane surface in the feed and the permeate sides, respectively. The contours are rendered at a different region at each side of the membrane. The high-velocity regions correlate with the higher temperature regions at the feed side of the membrane while the higher velocity regions correlate well with the low-temperature regions at the permeate side of the membrane. The higher flow rate alleviates the

temperature polarization in each module. The enhanced mixing translates to higher temperature over the surface of the membrane at the feed side. However, the higher mixing regions translate to the low values of temperature which is preferred at the permeate side for the low-level temperature polarization. At the permeate side, the low temperature is observed in the middle of the spacer cells and near the periodic surfaces at z/h = 0 and 5. The temperature distribution over the surface of the membrane at the feed side has the same signature as the velocity field shown in Fig. 11. The higher temperature regions are seen at the intersection of the spacer strands. The increase of the strand diameter of spacers increases the temperature at the feed side and decreases the temperature at the permeate side, and thus aids in mitigating the temperature polarization in the module. Table 7 lists the values of the average temperature polarization for the cases mentioned in Fig. 12.

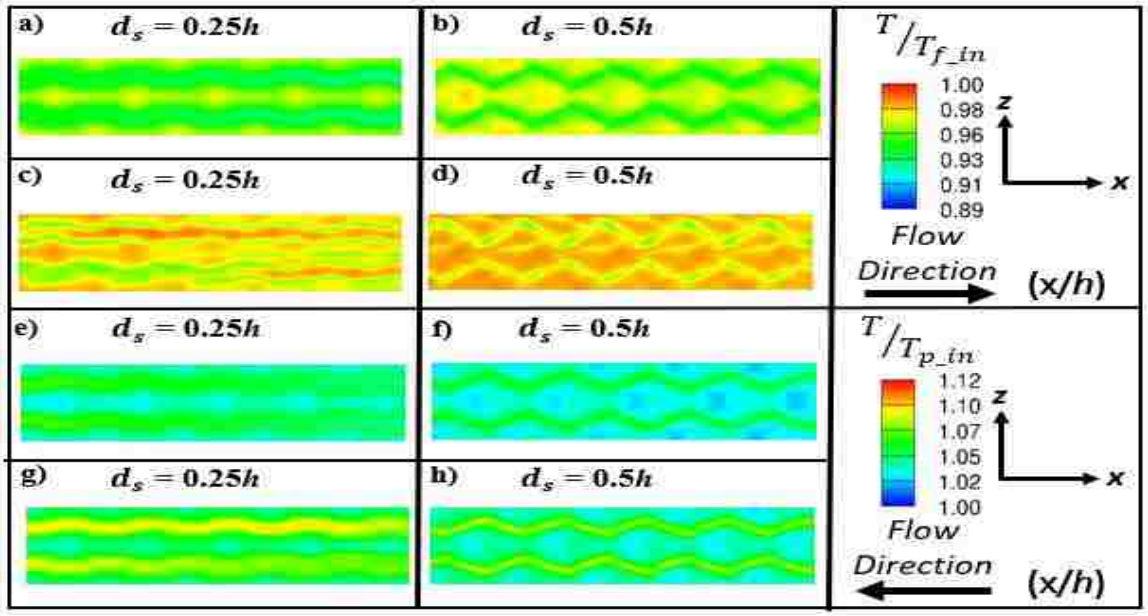

Figure 12. Contours of the normalized temperature along the membrane surface at the feed side for a) Re_f = 500 and d_s = 0.25h, b) Re_f = 500 and d_s = 0.5h, c) Re_f = 1500 and d_s = 0.25h, d) Re_f = 1500 and d_s = 0.5h, and at the permeate side for e) Re_f = 500 and d_s = 0.25h, f) Re_f = 500 and d_s = 0.5h, g) Re_f = 1500 and d_s = 0.25h, h) Re_f = 1500 and d_s = 0.5h. Images are rendered at 23 ≤ x/h ≤ 47 at the feed side and 15 ≤ x/h ≤ 35 at the permeate side.

The inlet concentration of the feed is selected as 0.035 [kg_{solute} /kg_{water}] to represent a typical sea-water desalination process. The concentration over the surface of the

membrane at the feed side increases in the stream-wise direction. The increase in the feed concentration is a result of the water vapor permeation from the feed to the permeate side. Ideally, the concentration ratio should be unity to avoid a concentration polarization. The concentration polarization is not a significant factor in DCMD systems since the vapor pressure, the driving mechanism of the vapor permeation, will not be influenced strongly by the concentration [59]. However, the fouling propensity over the membrane surface will increase with the concentration polarization, and that in turn reduces the vapor permeation over a long-time operation. Also, fouling reduces the life expectancy of membranes and adds extra maintenances costs. In the current simulations, the formation and the growth of fouling are not included in the mathematical model. Fig. 13 depicts the concentration polarization variation over the surface of the membrane in the developed region for all cases considered. Fig. 13(a) shows that higher values of concentration are present in the low-velocity regions. Also, the low concentration regions coincide with the high-velocity regions. As the flow rate is increased, the concentration polarization is reduced, as seen in Fig. 13(c). When the strand diameter is increased (Fig. 13(b) and 13(d)) the concentration polarization is mitigated further compared with the spacer of smaller diameter. The lowest concentration polarization is attained when the spacers diameter is $0.5h$ and Re_f = 1500. Table 7 shows the average concentration polarization values in the respective cases mentioned in Fig. 13.

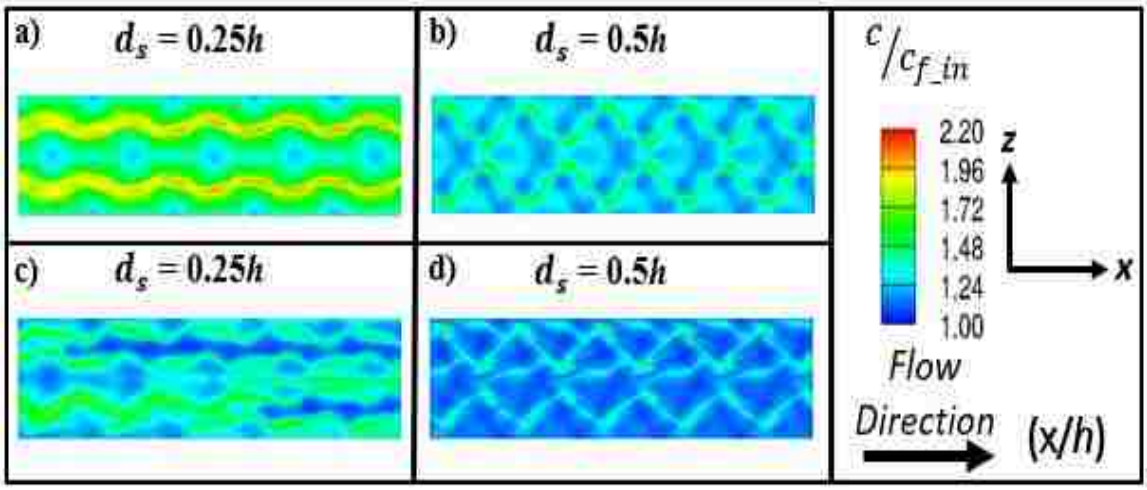

Figure 13. Contours of the normalized concentration along the membrane surface at the feed side for a) Re_f = 500 and d_s = 0.25h, b) Re_f = 500 and d_s = 0.5h, c) Re_f = 1500 and d_s = 0.25h, d) Re_f = 1500 and d_s = 0.5h.Images are rendered at 23 ≤ x/h ≤ 47.

It is important to calculate the shear stress over the membrane surface at the feed side. The shear stress can be related to the fouling/scaling and the concentration polarization over the membrane surface. As the shear stress increases, the concentration polarization is expected to be lowered. Fig. 14 shows the variation of the shear stress over the surface of the membrane at the feed side. The high shear stress regions seen in Fig. 14(a) correspond to the low concentration polarization region seen in Fig. 13(a). The shear stress increases with increasing the flow rate inside the channel, as shown in Fig. 14(c). Also, Fig. 14(b) and 14(d) shows that increasing the spacer strand diameter increases the shear stress. The shear stress is normalized with the maximum shear stress for each corresponding case. Table 2 lists the maximum shear stress values obtained for various values.

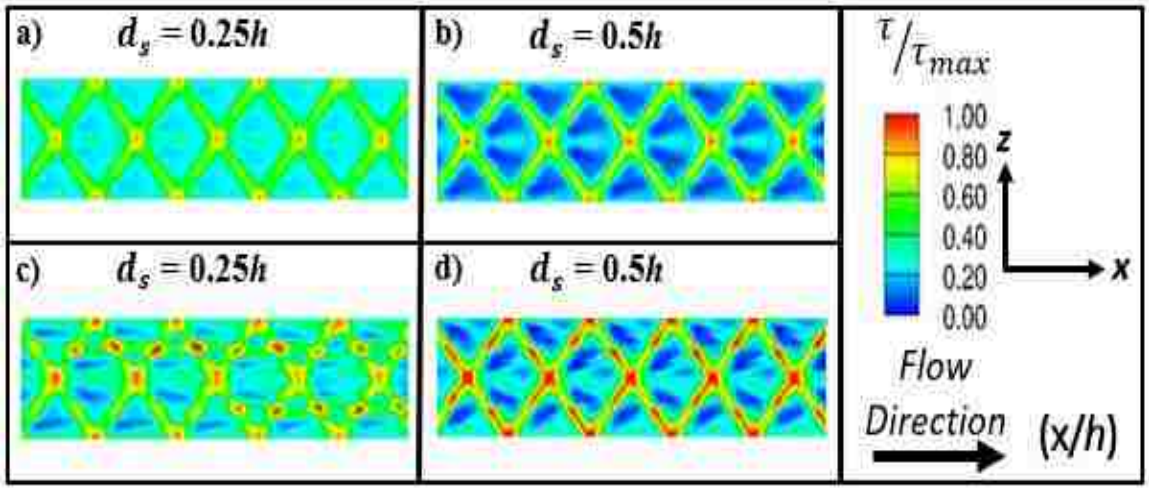

Figure 14. Contours of the normalized wall shear stress at the feed side for a) Re_f = 500 and d_s = 0.25h, b) Re_f = 500 and d_s = 0.5h, c) Re_f = 1500 and d_s = 0.25h, d) Re_f = 1500 and d_s = 0.5h.Images are rendered at 23 ≤ x/h ≤ 47

The suction rate through the membrane can be determined using the local temperature at each side of the membrane, the local concentration, and the membrane properties. The vapor pressure is a function of both the temperature and concentration. As the feed temperature increases, the vapor pressure at the feed side increases. Also, the low values of vapor pressure at the permeate side are desirable for better flux performance. Fig. 15 shows the variation of the suction velocity over the membrane surface. Fig. 15(a) shows the water flux contours for $d_s = 0.25h$ and $Re_f = 500$. The lowest values of suction velocity correspond to the low velocity regions observed in Fig. 11(a). Increasing the flow rate increases the suction velocity for each size of spacers. Also, increasing the spacer diameter increases the suction velocity at each flow rate, as seen in Fig. 15(b) and 15(d). The minimum and maximum values of local water vapor flux attained in the current simulations are 29 and 116 kg/m^2h, respectively. Table 7 shows the average water vapor flux values determined for all cases considered.

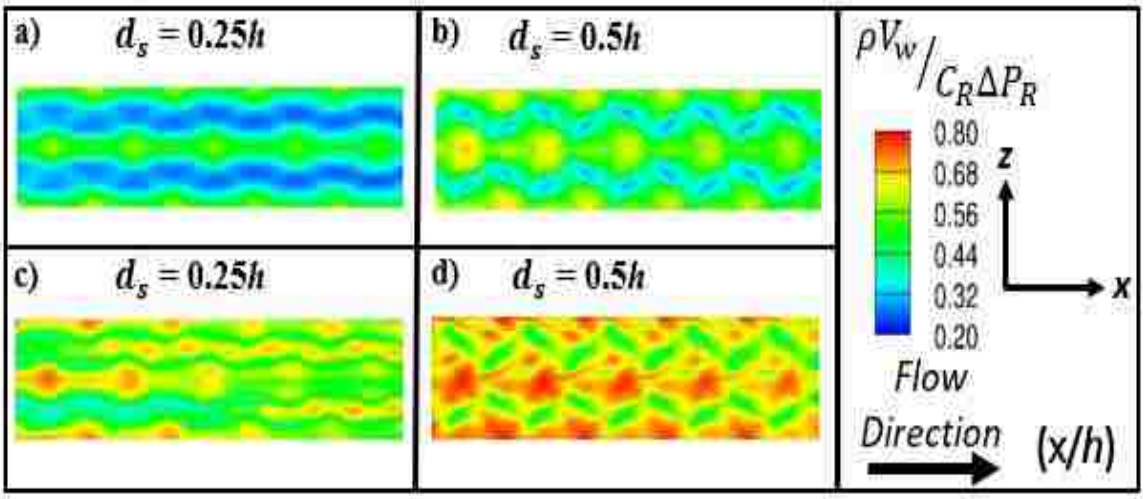

Figure 15. Contours of the normalized water flux for a) Re_f = 500 and d_s = 0.25h, b) Re_f = 500 and d_s = 0.5h, c) Re_f = 1500 and d_s = 0.25h, d) Re_f = 1500 and d_s = 0.5h.Images are rendered at 23 ≤ x/h ≤ 47.

Table 7 shows the average CPC and TPC over the membrane surface, maximum shear stress, and average water vapor flux for the feed Reynolds number of 500 and 1500 and the spacer strand diameter of 0.25h and 0.5h. The spacers with a strand diameter of 0.5h and 0.25h reduced the concentration polarization by 24.4% and 17.6%, respectively at Re = 1500, while the temperature polarization has been reduced by 30.4% and 21.7%. The higher level of wall shear stress is obtained in the module with a larger spacer strand diameter. The occurrence of fouling/scaling is less likely with the application of spacers in the feed channel. The permeate flux of the module containing larger diameter spacers is increased by 51% at Re_f= 1500 compared to the module without the spacers. Module containing 0.5h diameter spacers yields 12.5% larger vapor flux compared to the module containing 0.25h diameter spacers.

Table 7. The area-averaged concentration and temperature polarization coefficients, maximum shear stress, and the water flux in the module with and without spacers at various values of the feed stream Re_f

	Case					
	Empty		0.25*h* Spacers		0.5*h* Spacers	
Re	**500**	**1500**	**500**	**1500**	**500**	**1500**
CPC [-]	1.91	1.64	1.58	1.35	1.36	1.24
TPC [-]	0.44	0.46	0.49	0.53	0.56	0.6
Shear stress [Pa]	0.37	1.2	1.55	6	3.3	12.5
Flux$[kg/m^2h]$	47.81	59.05	57.26	79.29	67.26	89.22

The main energy input to any MD desalination system is in the form of heating and cooling. In DCMD systems, the feed solution is typically heated to a temperature between $50 - 80$ ℃ while the permeate fluid is cooled to a temperature between $20 - 25$ ℃. Pumping power is considered as auxiliary power, and it is usually ignored in the performance consideration. The total thermal power input for the feed solution is

$$\dot{Q}_f = \dot{Q}_{in} - \dot{Q}_{out} = \dot{m} c_p T_{in} - \rho c_p \int T\, u\, dA = \dot{Q}_c + \dot{Q}_v \tag{21}$$

where $\dot{m}$ is the mass flow rate of the feed water, c_p is the specific heat of water, and T_{in} is the inlet feed temperature, ρ is the density of the water in the feed channel, and u is the streamwise component of the velocity of the feed solution at the exit. The total thermal power input of the feed channel is transferred through the membrane by vaporization and the conduction and it will be equivalent to the thermal power input of the permeate channel to cool the permeate solution since the module is assumed to be well-insulated. The heat consumed by the evaporation is beneficial and it will increase only when the rate of water permeation increases. The pumping power requirement of the feed flow is calculated

$$\dot{P} = \Delta P\, A\, U_{f,ave}$$

where ΔP is the pressure drop and A is the cross-sectional area of the feed channel.

Table 8 shows the thermal power input of the feed solution in the module without and with the spacers at *Re* = 1500 and d_s = 0.5*h*. The conductive power loss in the module without and with spacers is 15.6 and 13.76% of the total thermal power input, respectively, revealing that the conductive losses are smaller compared to the heat transferred by the phase change in each module. The heat transfer by the vaporization increases in the module containing spacers since the rate of vapor permeation increases. The conductive heat transfer across the membrane is also increased by the presence of spacers due to the mixing effects. The pumping power is only a small fraction of the required heat input to the system in each module. Luo et al. [60] have reported that the pumping power is around 0.5% of the heat input to the DCMD module. The results reveal that the pumping power for the empty module and the module with spacers were 0.0022 and 0.013%, respectively. Results predicted by the energy analysis are consistent with results reported in the literature by the experimental studies, thus further validates the mathematical model and numerical methods.

Table 8. *Energy balance and pumping power for the DCMD system*

	$\dot{Q}_f\ [^{kW}/_{m^2}]$	$\dot{Q}_c[^{kW}/_{m^2}]$	$\dot{Q}_v\ [^{kW}/_{m^2}]$	$\dot{Q}_c/(\dot{Q}_c+\dot{Q}_v)$	$\dot{P}/\dot{Q}_f$
Empty	50.4	7.88	42.52	15.6%	0.0022%
Spacer	74.6	10.26	64.33	13.76%	0.013%

Conclusion

Three-dimensional steady-state simulations were conducted to investigate the effect of net-type spacer diameter on the performance of the DCMD system. In this study, the laminar model was used to simulate the desalination process in the module without the spacers, while $k-\omega\ SST$ turbulence model was used to simulate the process in modules containing spacers. The water vapor flux along the membrane surface is coupled with local

temperatures in the feed and the permeate channels and local concentration in the feed channel. The feed Reynolds number of 500 and 1500 are considered in the simulations while the permeate Reynolds number is fixed at 330. We demonstrated that the presence of spacers in the feed and permeate channel enhanced the CPC, TPC, and the flux. The DCMD module flux performance is enhanced more than 52% with the inclusion of spacers in the feed and permeate channel. Moreover, as the diameter of the spacer is increased from $0.25\ h$ to $0.5\ h$ the CPC, TPC, and the flux are improved by 13.9%, 14.2%, and 17.4% respectively at Re_f= 500. It is also shown that the spacers become more efficient when the flow rate in the feed channel is increased. It is also demonstrated that the conductive losses across the membrane are less than 16% of the total thermal power input of the module.

Chapter 5: Characterizing performance of the embedded-spacer membranes in direct contact membrane distillation modules

Computational fluid dynamics simulations were conducted in direct contact membrane distillation modules containing a novel spacer design. The net-type spacers with a 45° strand angle and various strand size were embedded between two active layers of the membrane. The embedded spacers create a micro-patterned surface at each side of the membrane that induces local mixing in the vicinity of the surface. The $k-\omega\ SST$ turbulent model was employed to conduct simulations in modules with embedded spacers while the laminar model was employed to conduct simulations in the module containing a flat membrane. The membrane was treated as a functional surface with zero thickness. Dusty-Gas model was applied to determine the vapor permeation rate coupled with the local temperature and concentration over the surface of the membrane. Concentration and temperature polarization were mitigated significantly and water flux was enhanced by about 40% with the module containing embedded spacers of the larger strand. It is demonstrated here that with mitigation of polarizations and reduction of scaling/fouling propensity direct contact membrane distillation modules containing embedded spacers could be a good candidate for seawater desalination and for treating highly concentrated non-volatile solutions.

Numerical Model, Convergence, and validation

Simulations were conducted in a three-dimensional module. The dimensions of each channel were 60h in length and 5h in width, where h is the height, as shown in Fig. 16. The spacers were inserted between two active membrane layers 7.5h away from the inlet and

the exit. The angle between the strand of the embedded spacer and the horizontal direction was 45°. Nine cells of spacers were considered in the computational domain with 5h spacing between successive cells. The spacer's strand diameter of D = 0.1h, 0.2h, and 0.3h was considered in the simulations. Table 9 lists membrane structural properties and operating conditions used in the simulations. The membrane used here was an active PTFE flat sheet membrane with a permeability value of $9.18 \times 10^{-7}\ kg/m^2 Pa\ s$ at the reference temperature and pressure. The permeability depends on the feed and the permeate temperature along the membrane surface, as displayed in Table 1. The simulations were conducted at flow rates corresponding to $Re_f =$ of 500 and 1500 and $Re_p =$ of 330 and 1500 for the feed and permeate channel, respectively. Reynolds number for each stream is calculated as

$$Re_n = (U_{n,ave}\ \rho_n\ d_{n,h})/\mu_n$$

where $U_{n,ave}$ is the average velocity at the inlet, and $n = f/p$ represents the properties of the feed and permeate stream, respectively. The hydraulic diameter is determined from $d_{n,h} = 2hw/(h + w)$

The inlet concentration of the feed solution, 0.035 kg_{solute} /kg_{water}, represents seawater desalination. The feed and permeate inlet temperature were set $353\ K$ and $293\ K$, respectively.

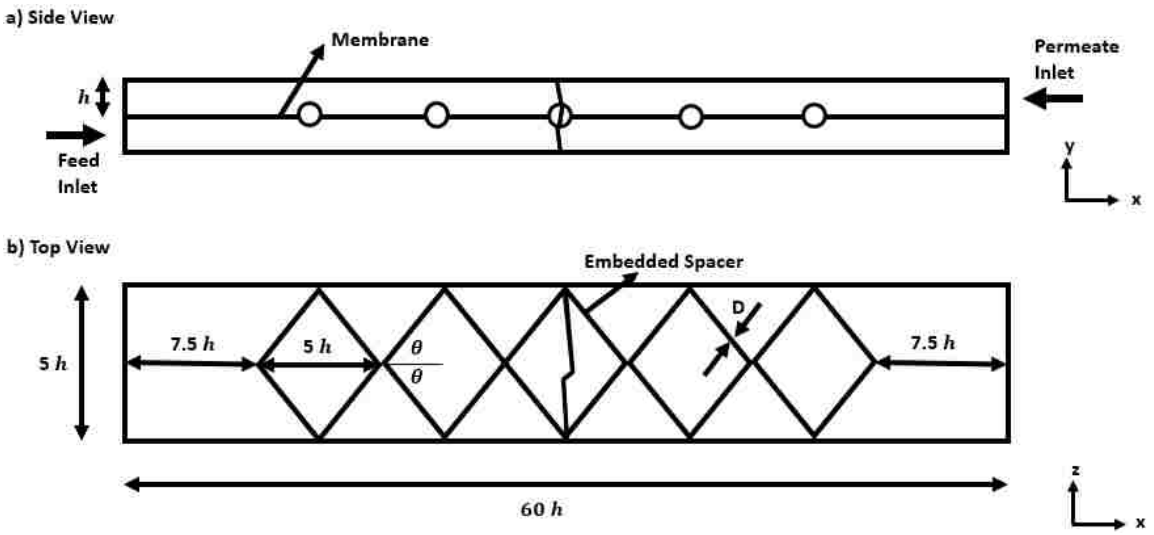

Figure 16. *Schematics of the module containing embedded spacers and dimensions of the geometry.*

Table 9. *Membrane properties and operating parameters used in the simulations*

Parameter	**Values**
Membrane thickness, δ	100 $[\mu m]$
Membrane porosity, ε	0.8 $[-]$
Membrane pore size, d_p	0.45 $[\mu m]$
Membrane tortuosity, τ	1.31 $[-]$
Membrane thermal conductivity, k_m	0.0285 [W/m K]
Feed Reynolds number, Re_f	500, 1500 $[-]$
Permeate Reynolds number, Re_p	330 $[-]$
Inlet feed concentration, $c_{f,in}$	0.035 $[\mathrm{kg_{solute}}/\mathrm{kg_{water}}]$
Inlet feed temperature, $T_{f,in}$	353 K
Inlet permeate temperature, $T_{p,in}$	293 K

The unstructured mesh was used to discretize the computational domain with an inflation layer near the membrane surface at each side of the membrane. The first layer thickness of 5 μm was employed to capture the concentration and temperature polarization [49]. A mesh independence study was conducted using mesh density of $N1$ = 10 million, $N2$ = 20 million, and $N3$ = 30 million elements for D = 0.3h and $Re_f = 1500$. Figure 17 shows profiles of the normalized stream-wise velocity (Fig. 17a) at z/h = 2 and y/h = 0.5, the normalized concentration (Fig. 17b) along the membrane at the feed side at z/h = 2, the normalized temperature along the membrane surface at the feed side (Fig. 17c), and the

permeate side (Fig. 17d) at z/*h* = 2. The velocity, concentration and temperature profiles obtained using *N*2 and *N*3 mesh density are nearly identical. It is demonstrated here that the mesh density *N2* is sufficient to ensure spatial convergence. Simulations were conducted using *N*2 = 20 million elements with y^+ = 0.6 achieved near the membrane surface is small enough to resolve boundary layers. Figure 18 shows a cross section of the mesh used in the simulations showing the refinement near the membrane surface and along the embedded spacers.

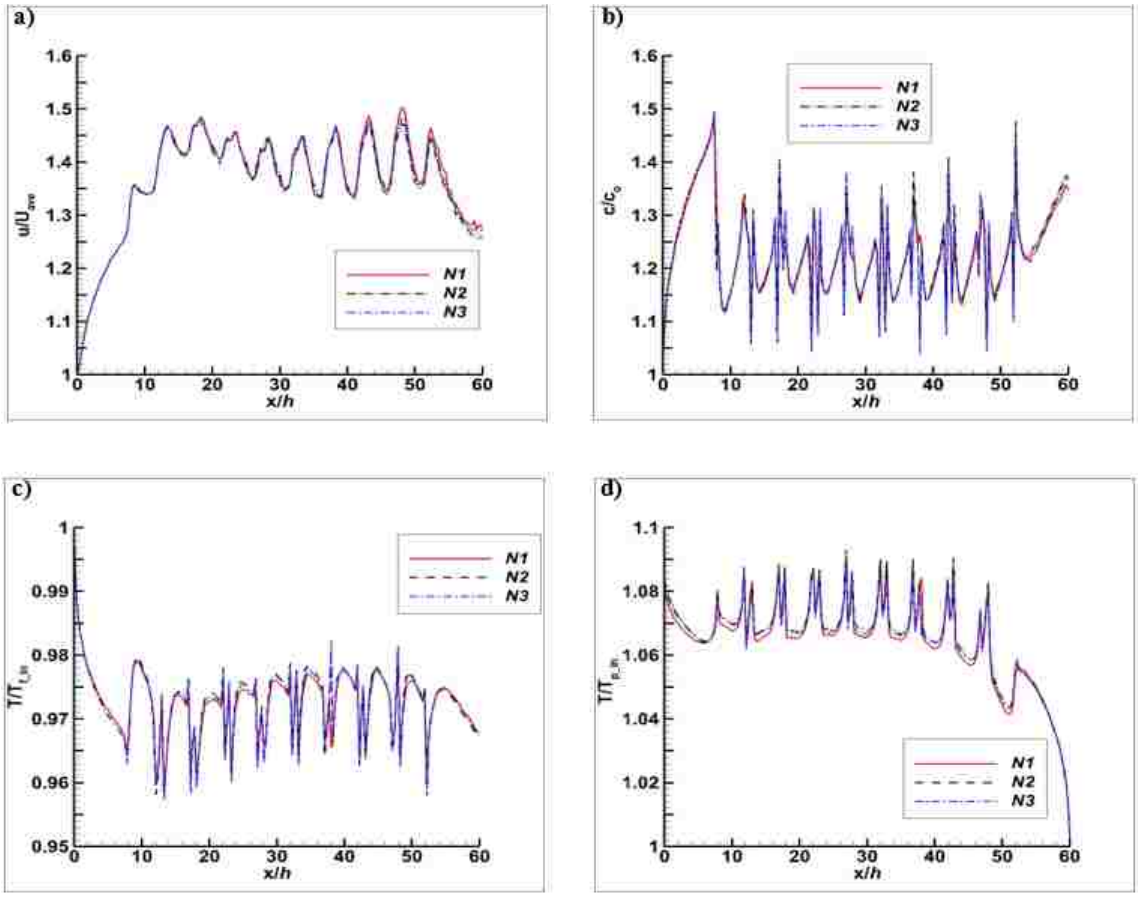

Figure 17. *Profiles of a) the stream-wise component of the feed velocity at z/* h *= 2 and y/*h *= 0.5, b) the normalized concentration over the surface of the membrane in the feed side at z/* h *= 2, c) the normalized temperature over the surface of the membrane in the feed side at z/* h *= 2, and d) the normalized temperature over the surface of the membrane in the permeate side at z/* h *= 2.*

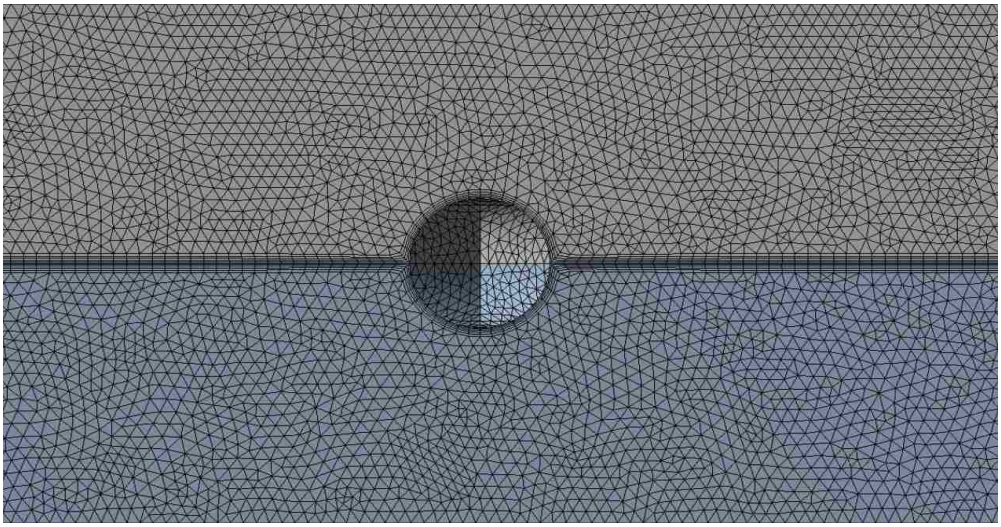

Figure 18. *A sample of the unstructured mesh for the geometry with embedded spacers.*

Results

In this work, the mathematical/physical model and the numerical method employed have been validated using the experimental data reported by [13] in a DCMD module without spacers. The inlet feed temperature was set to 80 ℃ with a salinity of 42,000 ppm. The flow rate in the feed channel was set to 1.5 L/min which corresponds to $Re_f = 12{,}500$, while the permeate water temperature was set to 20 ℃ with a flow rate of 1.5 L/min which corresponds to $Re_p = 4{,}800$. The difference in Reynolds number between the feed and the permeate flow is due to the variation of the fluid viscosity with temperature. The membrane thickness, porosity, tortuosity, and the pore size of the membrane were determined by examining the membrane using scanning electron microscopy (SEM) in Ref. [11,13] for two membranes designated by M1 and M2. The structural properties of each membrane are listed in Table 10.

Table 10. membrane properties for the two membranes used in the experimental work done by [13]

Parameter	M1	M2
Membrane thickness, δ $[\mu m]$	170	100
Membrane porosity, ε $[-]$	0.73	0.68
Membrane pore size, d_p $[\mu m]$	0.26	0.50
Membrane tortuosity, τ $[-]$	1.25	1.31

Validation simulations were conducted in the DCMD module without spacers using 3.5 million and 7 million elements to ensure the mesh independence of the validation test. The mesh near the membrane surface was refined with the first layer thickness of the mesh was set to $5 \times 10^{-6}\, m$ to resolve the temperature and concentration boundary layers attached to the surface of the membrane. The flow field predicted by $k-\omega$ SST turbulent model using 3.5 and 7 million mesh elements was nearly identical. The y^+ values near the membrane surface for the 3.5 million and the 7 million mesh elements were 0.65 and 0.50, respectively. We presented the validation results obtained with 7 million mesh elements.

The water vapor flux predicted was compared against the measured data reported in [13]. For membrane M1, the reported water flux was $60\ kg/m^2h$ while the water vapor flux predicted by the present study was $63\ kg/m^2h$. For membrane M2, the reported and predicted water vapor flux was $89\ kg/m^2h$ and $97\ kg/m^2h$, respectively. The water vapor flux predicted and measured for M1 and M2 membrane agreed within 5% and 8.9% deviation, respectively, and thus the mathematical model and the numerical method employed were validated.

Results are presented for the set of operating conditions and the fixed structural properties of the membrane, as listed in Table 9. The diameter of the embedded spacers was varied: $0.1h$, $0.2h$, and $0.3h$, where h is the height of the feed and the permeate channel.

Figures 19 and 20 depict the flow field inside the feed channel for Re_f = 500, 1500, $Re_p = 330$, and D = 0.1h, 0.2h and 0.3h. The contours of the normalized stream-wise velocity are rendered at y/h = 0.8 plane, while the iso-surfaces of the Q-criterion are rendered inside the feed channel. In all modules, the velocity field is repeated following the cells of embedded spacers, as depicted in Figure 19. The stream-wise velocity is nearly uniform for D = 0.1h, as shown in Fig 19(a and b). The velocity field is altered slightly by the presence of the small diameter embedded spacers. The vortical activities are confined into regions downstream vicinity of spacers and near the channel wall. The level of mixing induced by embedded spacers is minor. For D = 0.2h, the imprint of spacers is observed in the velocity contours. The influence of spacers on the velocity field is small for $Re_f = 500$, and more pronounced for $Re_f = 1500$. Higher velocity is observed inside the spacer cells over the membrane surface. The vortical activities become more intense downstream of spacers while the regions near the forward intersection of strands are lack of vortical activities. The rolls of vortices expand into the middle region of cells, as seen in Fig. 20(c and d). The level of mixing increases inside the module containing the embedded spacers of 0.2h diameter. For D = 0.3h, the effect of the spacers on the velocity field becomes even stronger. The high and low velocity regions are more visible. The vortical activities are intensified inside the module containing 0.3h diameter strands. The large and small vortex filaments observed within the cell become stronger. The elevated mixing in the module with a larger size strand of embedded spacers would aid in eliminating the temperature and concentration polarization and enhancing the flux performance of the module.

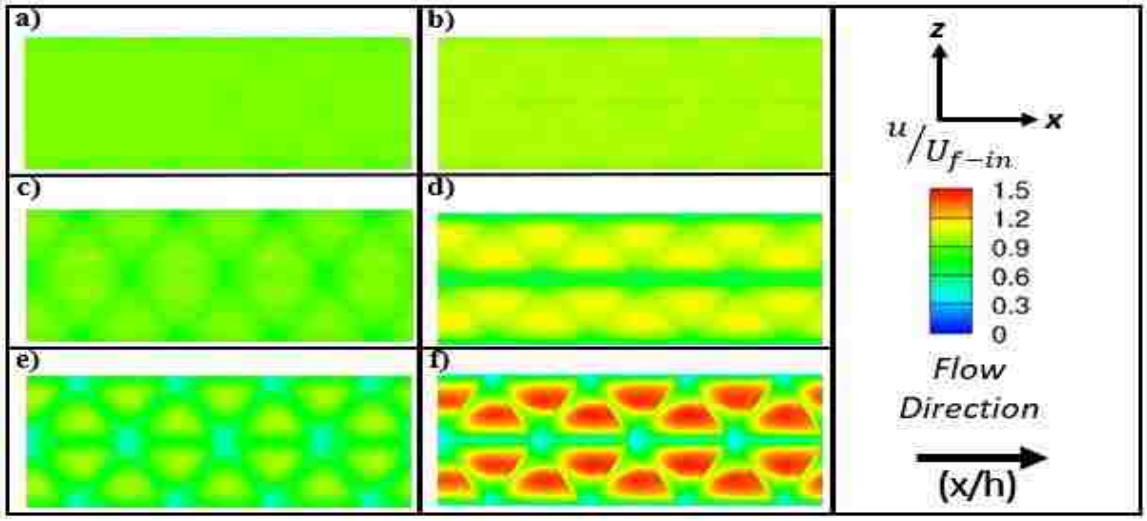

Figure 19. *Contours of the normalized stream-wise velocity in the feed channel at y/h = 0.8 for* a) Re_f = 500 and D = 0.1h, b) Re_f = 1500 and D = 0.1h, c) Re_f = 500 and D = 0.2h, d) Re_f = 1500 and D = 0.2h, e) Re_f = 500 and D = 0.3h, f) Re_f = 1500 and D = 0.3h. Images are rendered at 28 ≤ x/h ≤ 47.

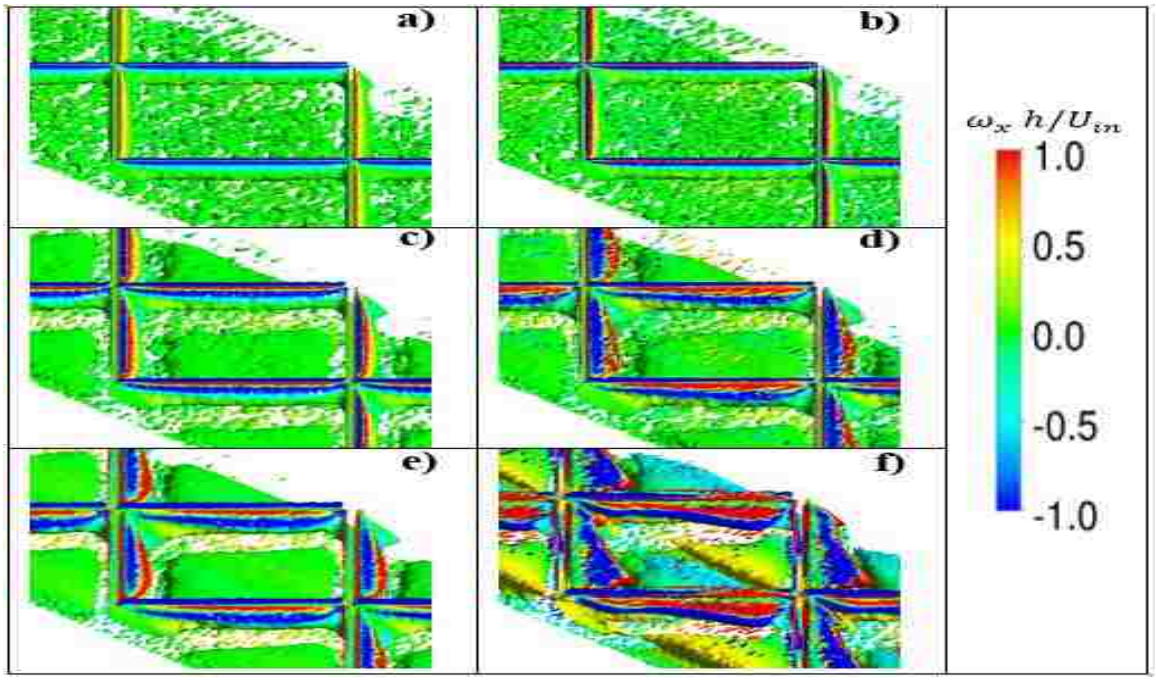

Figure 20. Iso-surfaces of the normalized Q-criterion at a level of 0.01 plotted in the feed channel for a) Re_f = 500 and D = 0.1h, b) Re_f = 1,500 and D = 0.1h, c) Re_f = 500 and D = 0.2h, d) Re_f = 1,500 and D = 0.2h, e) Re_f = 500 and D = 0.3h, f) Re_f = 1,500 and D = 0.3h. Images are rendered at 31 ≤ x/h ≤ 40.

Figure 21 shows contours of the normalized concentration over the membrane surface in the feed channel for $Re_f = 500, 1500$, $Re_p = 330$, and D = 0.1h, 0.2h and 0.3h. The concentration is normalized by the inlet feed concentration. With the water vapor permeating through the membrane from the feed to permeate stream, the salt accumulates

over the membrane surface and the concentration boundary layer is formed. The phenomenon is referred to as the concentration polarization. The concentration polarization would cause the scaling and fouling over the surface of the membrane, and it is detrimental to module flux performance. The mitigation of concentration polarization can be achieved by promoting a good mixing to disrupt the growth of the boundary layer. In the current study, the innovative idea of embedded spacers is employed to induce mixing with a minimal pressure drop in both channels. It should be noted that the embedded spacers are modeled as impermeable rods, and no water vapor would cross the embedded spacer structure. The white regions in the contours shown in Fig. 21 correspond to the location of the embedded spacers. The higher concentration is observed in the middle of the membrane near the intersection of strands. The high concentration regions (regions with an elevated level of concentration polarization) coincide with regions of lower vortical activities. The concentration polarization is mitigated downstream of the strand inside the cell. For each flow rate, the intensity of concentration polarization is reduced as the strand diameter is increased. For a given strand size, the level of polarization is reduced as the flow rate is increased, as depicted in Fig. 21. The upstream location where the strands of the embedded spacer intersect has a higher propensity to scaling/fouling. For D = $0.3h$ and $Re_f = 1500$, the normalized concentration tends to unity, and thus the ideal operation condition regarding the concentration polarization is approached.

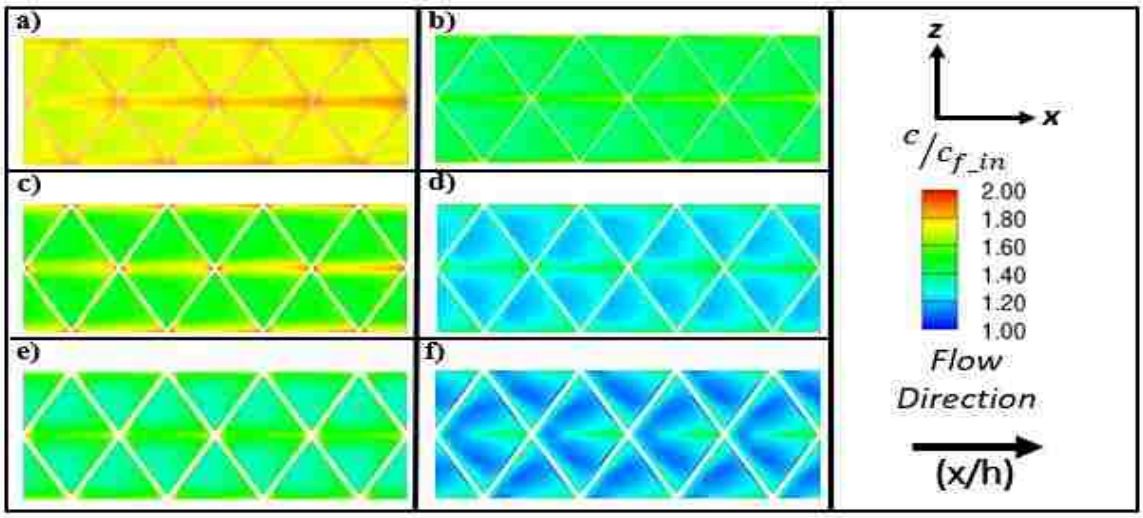

Figure 21. Contours of the normalized concentration along the membrane surface at the feed side a) Re_f = 500 and D = 0.1h, b) Re_f = 1500 and D = 0.1h, c) Re_f = 500 and D= 0.2h, d) Re_f = 1500 and D = 0.2h, e) Re_f = 500 and D = 0.3h, f) Re_f = 1500 and D = 0.3h Images are rendered at 28 ≤ x/h ≤ 47.

Figure 22 shows the local variation of the normalized concentration along the surface of the membrane at the feed side for $Re_f = 1500$, $Re_p = 330$, and D = 0.1h, 0.2h and 0.3h. The concentration profiles are compared to that obtained in the module containing membrane without embedded spacers. The presence of the embedded spacers disrupts the growth of the concentration boundary layer, and thus mitigates the concentration polarization. In the module with a flat membrane, the concentration increases monotonically in the stream-wise direction while it displays a wavy structure with a wavelength of the cell length in the module with an embedded spacer membrane. For the smallest size strand (D = 0.1h), the cell-averaged amplitude of the normalized concentration increases slightly in the flow direction. The small size spacer is not very effective mitigating the concentration polarization, even though the level of polarization is still reduced significantly compared to that in the module with a flat membrane. As the strand diameter is increased, the level of concentration is reduced and the cell-averaged amplitude of the wavy profile becomes constant; meaning that the level of concentration polarization becomes independent of the length of the module.

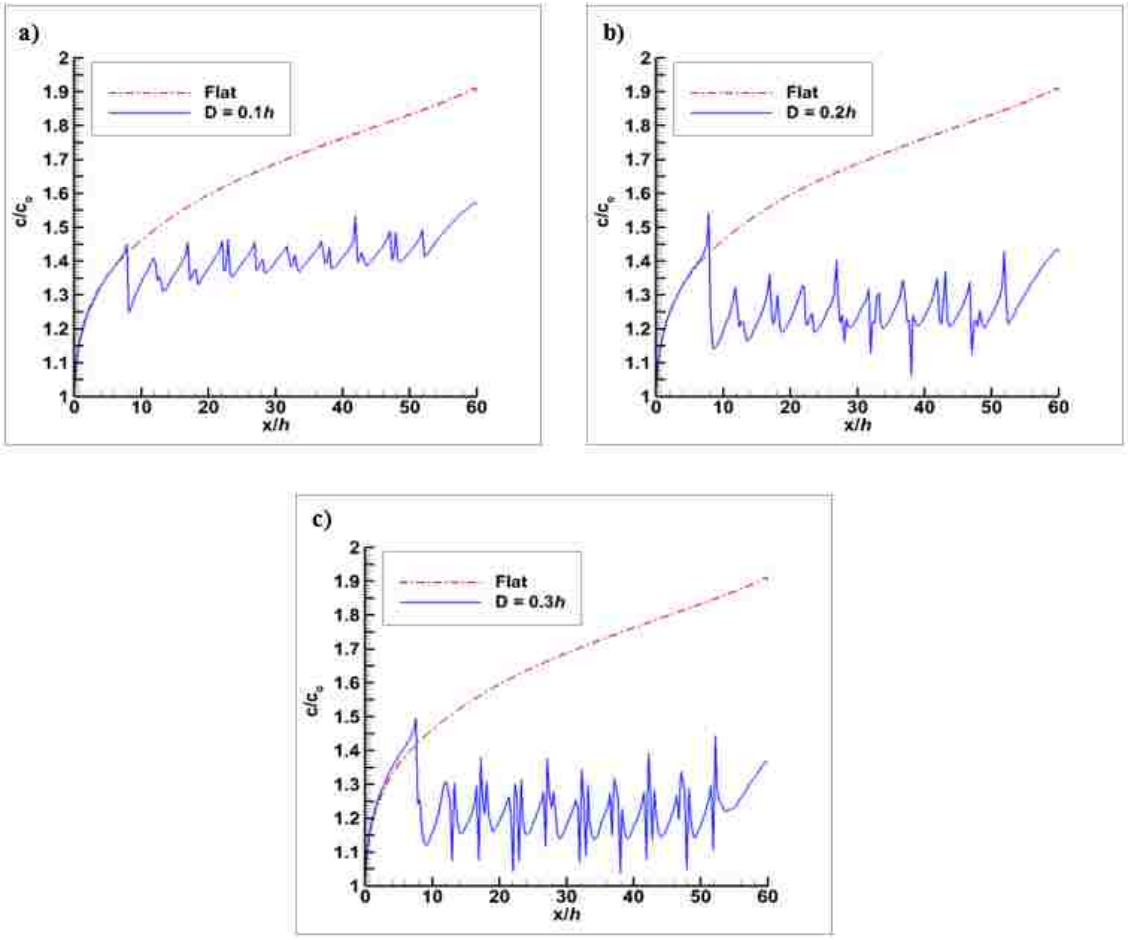

Figure 22. Profiles of the normalized concentration along the membrane surface at the feed side at z/h = 2 for Re_f = 1500. Concentration profiles are acquired in the module containing spacers of strand diameter a) D = 0.1h, b) D = 0.2h, c) D= 0.3h and are compared to that obtained in the module containing membrane without embedded spacers.

Figure 23 shows contours of the normalized temperature over the membrane surface at the feed side for $Re_f = 500, 1500$, $Re_p = 330$, and D = 0.1h, 0.2h and 0.3h. The temperature is normalized with the inlet feed temperature. Maintaining high local temperature difference across the membrane is vital since the vapor flux permeating through the membrane is driven by the vapor pressure difference that increases with the increasing temperature difference. The temperature of the feed solution decreases as the water vaporizes over the membrane surface at the feed side. Also, the heat transfers by conduction from the feed to permeate channel through the membrane decreases the temperature of the feed solution. It should be noted that the latent heat of vaporization

accounts for nearly 80% of the total heat transfer in the DCMD module studied. With the heat transfer from the feed to the permeate channel, the thermal boundary layer will be formed at each side of the membrane. The phenomenon is called as the temperature polarization. It is vital to minimize the temperature polarization within the module since it decreases the water permeation rate by reducing the driving temperature difference across the membrane. When there is a poor mixing in the feed channel, the temperature of the solution away from the membrane surface will be much greater. Ideally, the temperature of the feed and permeate solution near the membrane surface would be close to their inlet temperature. The mixing promoters aid in reaching the ideal operating conditions by mitigating temperature polarization.

The effect of the spacers on temperature distribution along the membrane surface is not strong at the low flow rate, as shown in Fig. 23(a, c, e) for D = 0.1h, 0.2h, and 0.3h with $Re_f = 500$. The temperature is elevated along the surface of the membrane at the higher flow rate. For D = 0.2h, the temperature is increased significantly inside each cell except in a thin layer connecting the intersection of the strands. The temperature is also lower in a small region downstream of strands, as shown in Fig. 23d. As the strand diameter is increased further to D = 0.3h, the feed temperature inside the cell tends to unity (see Fig. 23f); approaching an ideal operating condition regarding temperature polarization.

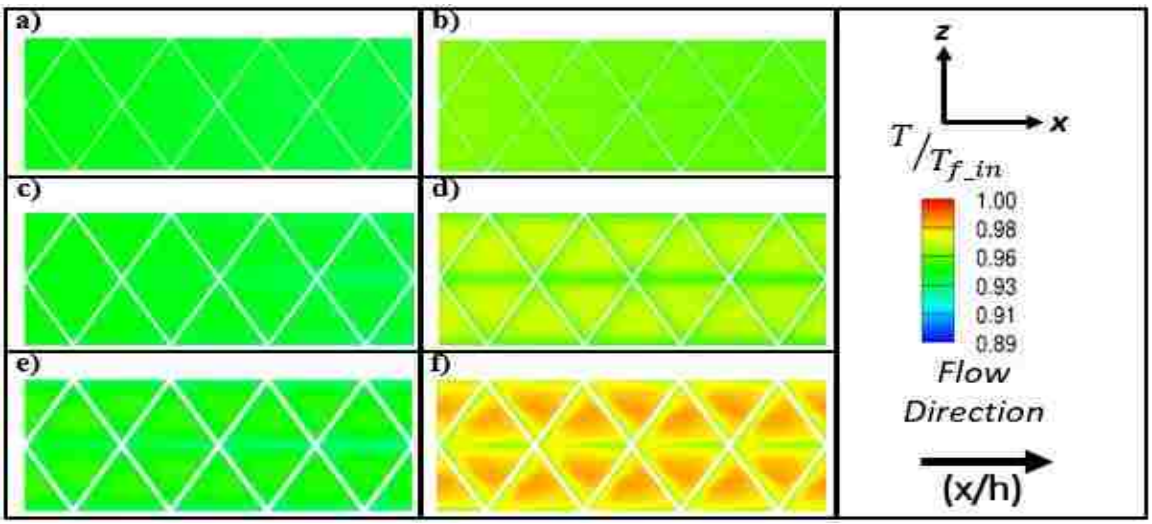

Figure 23. Contours of the normalized temperature along the membrane surface at the feed side for a) Re_f = 500 and D = 0.1h, b) Re_f = 1500 and D = 0.1h, c) Re_f = 500 and D= 0.2h, d) Re_f = 1500 and D = 0.2h, e) Re_f = 500 and D = 0.3h, f) Re_f = 1500 and D = 0.3h Images are rendered at 28 ≤ x/h ≤ 47.

Figure 24 shows local temperature variations over the membrane surface at a location of z/h = 2 for $Re_f = 1500$, $Re_p = 330$, and D = 0.1h, 0.2h and 0.3h. Temperature profiles are compared to that obtained in the module containing membrane without embedded spacers. In the module with a flat membrane, the temperature of the feed solution at the membrane surface decreases monotonically in the stream-wise direction, while temperature profiles display a wave pattern following the cells of embedded spacers. For D = 0.1h, the cell-averaged temperature is elevated slightly, but it stills decreases in the flow direction with a constant slope, as shown in Fig. 24a. For D = 0.2h, the temperature over the membrane surface fluctuates with a nearly constant cell-averaged amplitude, as shown in Fig. 24b. The average amplitude of temperature fluctuations over the membrane surface is closer to the unity for D = 0.3h; demonstrating that the temperature polarization is mitigated significantly. It is also shown that the temperature polarization within the module containing embedded spacers of larger strand becomes independent of the length of the module at higher flow rates. Hence, the module flux performance becomes

independent of the length of the module. The performance reduction with increased module length is a major drawback of DCMD systems lacking a proper mixing.

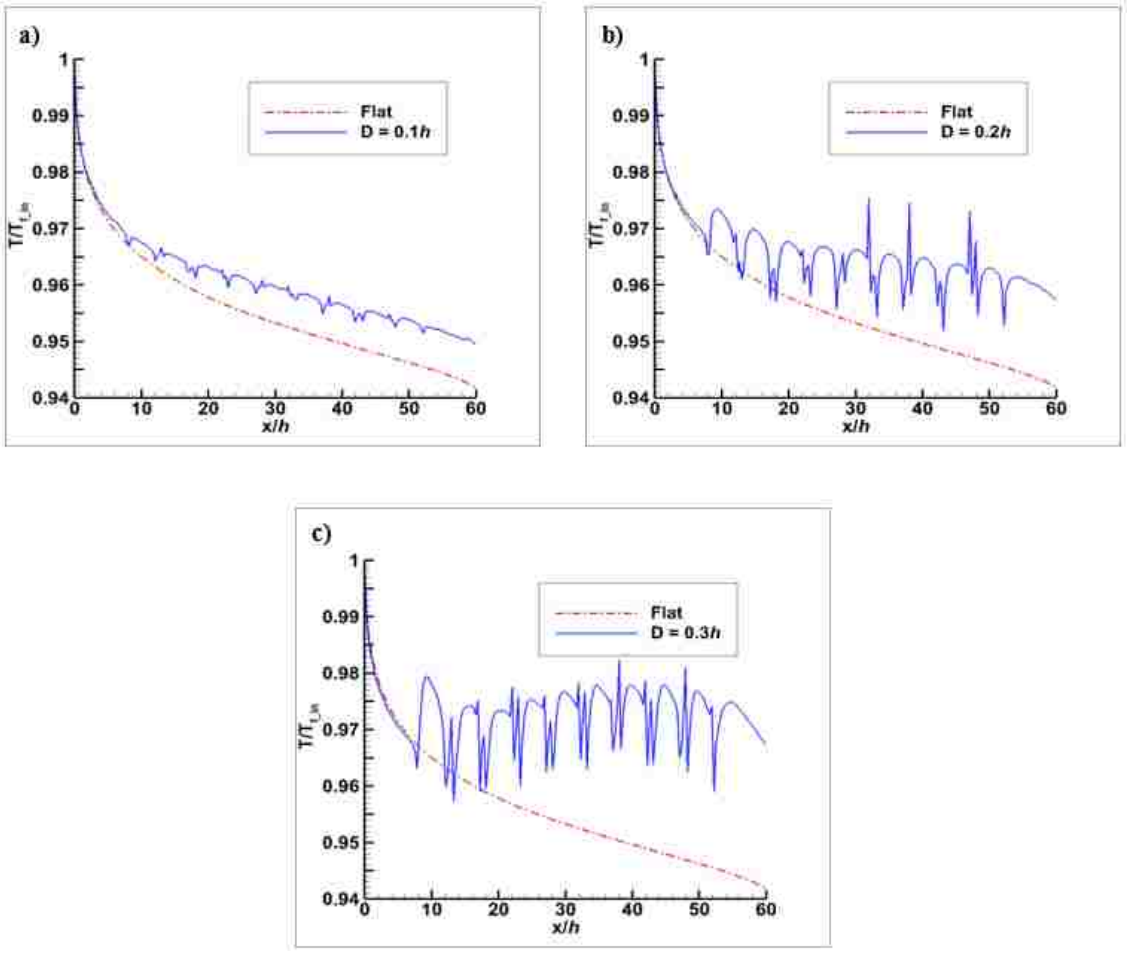

Figure 24. Profiles of the normalized temperature along the membrane surface at the feed side at z/h = 2 for Re_f = 1500. Temperature profiles are acquired in the module containing spacers of strand diameter a) D = 0.1h, b) D = 0.2h, c) D= 0.3h and are compared to that obtained in the module containing membrane without embedded spacers

Figure 25 shows contours of the normalized temperature over the membrane surface in the permeate channel for $Re_p = 330, 1500$, $Re_f = 1500$, and D = 0.1h, 0.2h and 0.3h. The temperature was normalized with the inlet permeate temperature. The permeate stream should be maintained at the low temperature for better system performance, and the normalized temperature of unity represents the ideal operating condition regarding to

temperature polarization. For $Re_p = 330$, the temperature increases as the strand size of the spacer is increased, as shown in Fig. 25(a,c,e). The flow rate of $Re_p = 330$ is too low to promote mixing in the permeate channel, and thus the intensity of temperature polarization at the permeate side increases as the rate of vapor permeate is increased in modules with a larger strand diameter. We notice a significant improvement in the temperature polarization at $Re_p = 1500$, as shown in Fig. 25(b,d,f). The temperature over the surface of the membrane approaches unity for $Re_p = 1500$ and D = 0.3h. It is important to note that the vapor pressure difference is more sensitive to the decrease in the feed solution temperature than the increase in the permeate solution temperature.

Figure 26 shows the local permeate temperature variation over the membrane surface at a location of z/h = 2 for $Re_f = 1500$ and D = 0.1h, 0.2h and 0.3h. Temperature profiles in the module containing embedded spacers show a wavy pattern with a wavelength of the spacer cell length, while the temperature in the module with a flat membrane increases monotonically. The permeate surface temperature is reduced significantly by the presence of embedded spacers of a larger strand.

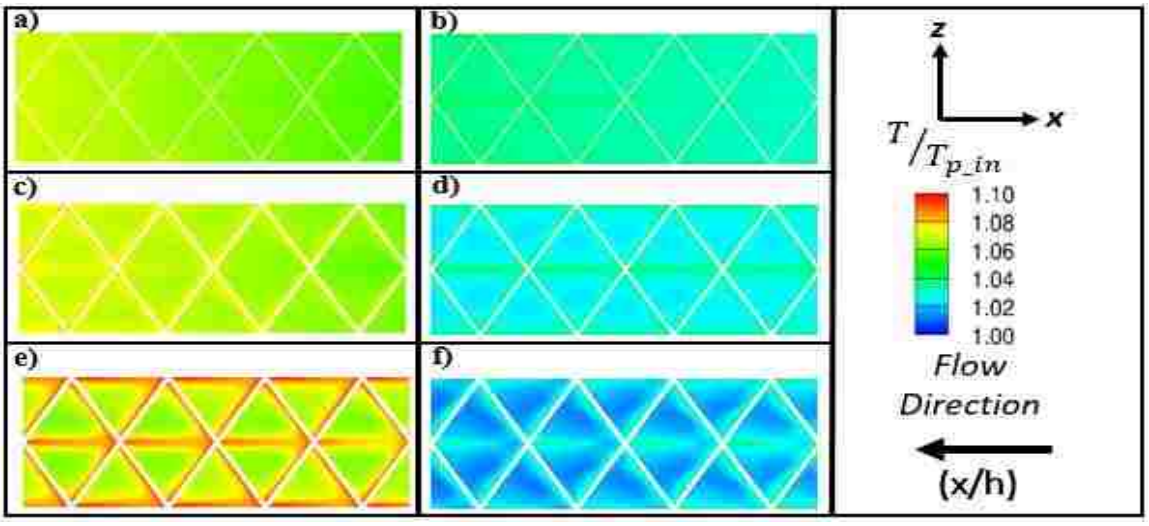

Figure 25. Contours of the normalized temperature along the membrane surface at the permeate side for a) $Re_p = 330$ and D = 0.1h, b) $Re_p = 1500$ and D = 0.1h, c) $Re_p = 330$ and D = 0.2h, d) $Re_p = 1500$ and D = 0.2h, e) $Re_p = 330$ and D = 0.3h, f) $Re_p = 1500$ and D = 0.3h. Images are rendered at 18 ≤ x/h ≤ 37 for $Re_f = 1500$.

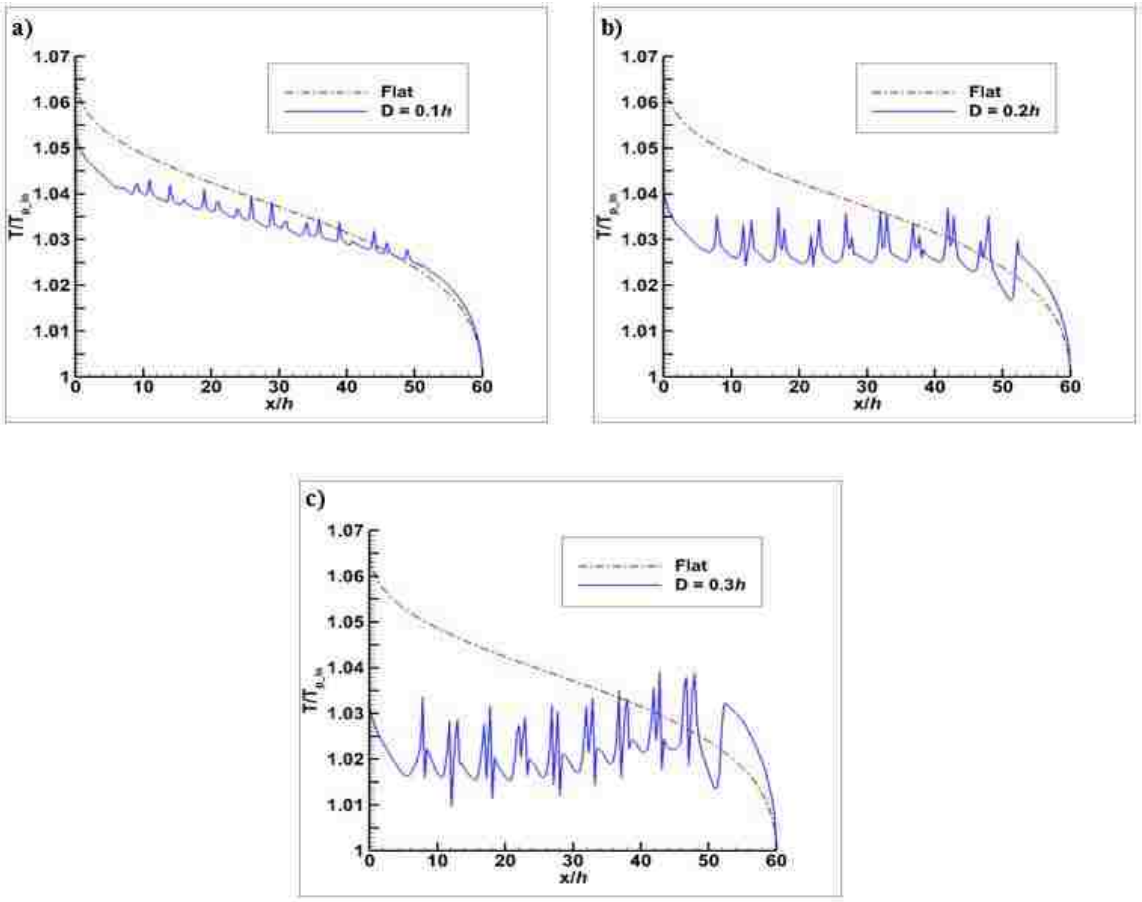

Figure 26. *Profiles of the normalized temperature along the membrane surface at the permeate side at z/h = 2 for $Re_p = 1500$ and $Re_f = 1500$. Temperature profiles are acquired in the module containing spacers of strand diameter a) D = 0.1h, b) D = 0.2h, c) D= 0.3h and are compared to that obtained in the module containing membrane without embedded spacers.*

Figure 27 shows the normalized shear stress over the membrane surface at the feed side for $Re_f = 500, 1500$, $Re_p = 330$, and D = 0.1h, 0.2h and 0.3h. The wall shear stress was normalized with the maximum shear stress obtained for each geometry and flow rate. The wall shear stress distribution is an indicator of the scaling/fouling inclination over the membrane surface [47]. Regions with low wall shear stress are more susceptible to scaling/fouling. The induced wall shear stress by the embedded spacer increases strongly as the strand diameter is increased. The wall shear stress is also increased profoundly as

the flow rate is increased within each separation module. The high shear stress regions correlate well with the high-speed regions. The low shear stress regions are observed in the wake of strands near their intersection, and these small spots are more prone to scaling/fouling.

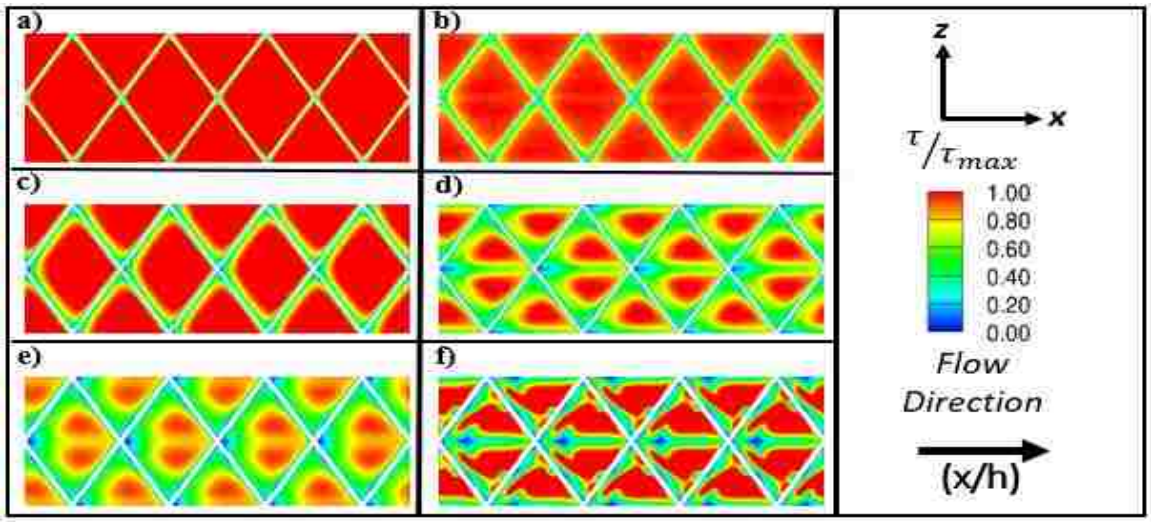

Figure 27. Contours of the normalized wall shear stress at the feed side for a) Re_f = 500 and D = 0.1h, b) Re_f = 1500 and D = 0.1h, c) Re_f = 500 and D= 0.2h, d) Re_f = 1500 and D = 0.2h, e) Re_f = 500 and D = 0.3h, f) Re_f = 1500 and D = 0.3h Images are rendered at 28 ≤ x/h ≤ 47. The value of τ_{max} (Pa) is a) 0.41, b) 1.3, c) 0.46, d) 1.5, e) 0.53, and f) 1.9.

Figure 28 shows the contours of the water vapor flux over the membrane surface. The suction velocity is normalized with a reference value calculated based on the inlet feed and permeate temperature and feed concentration. The reference suction velocity is a maximum permeation rate that is determined from the maximum vapor pressure difference for a selected operational condition. The suction velocity contours rendered at 28 ≤ x/h ≤ 47 exhibit a repeated structure indicating that the module flux performance is independent of the separation module length. The presence of the embedded spacers promotes mixing and enhances the water vapor flux. The spacers are considered impermeable, and the white regions in the contours represent the location of the embedded spacers. For $Re_f = 500$, the effect of the embedded spacers on the flux performance is not strong. The area-averaged

suction rate increases from about 30% to 40% of the reference suction velocity as the strand diameter is increased from 0.1h to 0.3h, as shown in Fig. 28(a,c,e). For $Re_f = 1500$, the effect of the spacer is profound. The permeate flux has reached up to 70% of the maximum reference value inside the cells for D = 0.3h, as depicted in Fig. 28(f). The small strips in the middle of cells connecting the intersection of the strand and the small regions downstream of the strands have lower flux. These regions have the lowest mixing and correlate well with regions with lower vortical activities, as illustrated in Fig. 20.

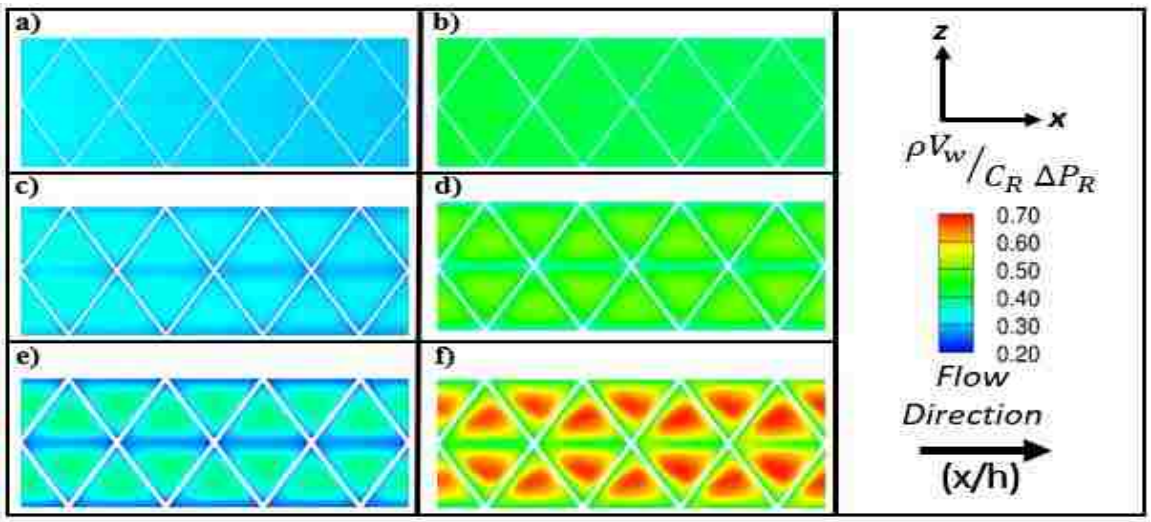

Figure 28. Contours of the normalized water vapor flux for a) $Re_f = 500$ and D = 0.1h, b) $Re_f = 1500$ and D = 0.1h, c) $Re_f = 500$ and D= 0.2h, d) $Re_f = 1500$ and D = 0.2h, e) $Re_f = 500$ and D = 0.3h, f) $Re_f = 1500$ and D = 0.3h. Images are rendered at 28 ≤ x/h ≤ 47 for $Re_p = 330$.

Table 11 shows a summary of the results presented in this study. The effect of the strand diameter of embedded spacers and the feed flow rate on the system performance were examined. The metrics used to assess the DCMD system performance were the average flux over the membrane surface, the temperature and concentration polarization coefficient, and the shear stress over the membrane surface.

The embedded spacers have a strong influence on concentration and temperature polarization. The embedded spacers induce localized mixing near the membrane surface, thus aid in mitigating the concentration and temperature polarization. The wall shear stress was elevated with the presence of the spacers, which would help in reducing the scaling/fouling inclination. More prominently, the vapor flux was enhanced with the presence of the spacers. The water flux was increased by about 40% in a module containing spacers with a strand diameter of $0.3h$ compared to that in the module with a flat membrane at $Re_f = 1500$ and $Re_p = 1500$. The mitigation of polarization and reduction of scaling propensity would make DCMD systems with embedded spacers suitable treating highly concentrated non-volatile feed solutions.

Table 11. The area-averaged concentration and temperature polarization coefficients, maximum shear stress, and the water flux (J: $kg\ m^{-2}h^{-1}$) in the module with and without embedded spacers at various feed and permeate flow rates.

Re_f, Re_p	500, 330				1500, 330				1500, 1500			
	CPC	**TPC**	J	**% Δ J**	**CPC**	**TPC**	J	**% Δ J**	**CPC**	**TPC**	J	**% Δ J**
Flat	1.91	0.44	47.81	-	1.64	0.46	59.05	-	1.67	0.55	62.24	-
D= 0.1h	1.7	0.45	49.64	3.8	1.41	0.47	64.08	8.52	1.46	0.59	67.89	9.1
D= 0.2h	1.55	0.45	50.32	5.25	1.28	0.48	68.58	16.14	1.31	0.64	73.75	18.5
D= 0.3h	1.44	0.47	52.71	10.25	1.24	0.51	80.31	36	1.27	0.71	86.8	39.46

Conclusion

In this work, the flux performance and polarization characteristics of DCMD modules containing the novel design of embedded spacers were studied using computational fluid dynamics simulations. The Navier-Stokes, energy, and scalar transport equations were solved with a coupled membrane flux conditions by employing the laminar model in DCMD module containing a flat membrane and $k-\omega\ SST$ turbulence model in modules containing embedded spacers. The mathematical model and numerical method were validated using existing experimental results. The membrane properties were set based on

the optimum membrane properties that are well-documented in previous studies, while the feed and permeate flow rate and the size of the spacer strand were varied. Net-type spacers of 45° filament angle, and $0.1h$, $0.2h$, and $0.3h$ strand diameter were selected. The feed flow rate of $Re_f = 500$ and 1500 and the permeate flow rate $Re_p = 330$ and 1500 were considered. The inlet temperatures of the feed and the permeate were $353\ K$ and $293\ K$, respectively, and the inlet concentration of the feed solution was set to 35,000 ppm representing seawater desalination processes.

Concentration polarization is a major drawback of membrane separation systems. The polarization reduces the membrane flux performance and causes scaling/fouling over the membrane surface, and so could result in disruption of the process. In MD systems, both temperature and concentration polarization could occur. The novel idea of the embedded spacers placed between active layers of the membrane was introduced to help to create local mixing near the membrane surface. The micro patterns created by the spacers disrupted the boundary layers attached to the membrane surface and thus mitigated polarizations. It was demonstrated here that the embedded spacer membranes could effectively be used in DCMD modules to mitigate the temperature and concentration polarization significantly. The flux enhancement was about 40% at the higher flow rates ($Re_f = 1500$, $Re_p = 1500$) while it was about 10% at the lower flow rates ($Re_f = 500$, $Re_p = 330$).

Chapter 6: LES simulation in DCMD module containing spacers

Computational fluid dynamics simulations were conducted to investigate the effects of the transient and steady state simulations in three-dimensional direct contact membrane distillation modules containing net-type spacers. The net-type spacers of $45°$ angle are placed in the middle of the feed and permeate channel. The net type spacers of diameter $0.5h$ were considered, where h is the height of each channel. The inlet temperature of the feed and the permeate channel set to $353\ K$ and $293\ K$. The feed Reynolds number Re_f is 1500 while the permeate Reynolds number Re_p is 330. A typical seawater concentration is used in the feed channel. The membrane properties are similar to the once listed in Table 9. Water vapor flux through the membrane is modeled using a Dusty-Gas model in which the rate of water vapor permeate is coupled with the local feed and permeate temperature and feed concentration along the surface of the membrane. The k-ω SST turbulence model is utilized for the steady state simulations while LES turbulence model is utilized for the transient simulations. The module-averaged water permeation rate predicted by LES turbulence model is only 2% higher than the flux predicted by k-ω SST turbulence model. This study demonstrates that the k-ω SST turbulence model is sufficient to model the turbulence flow in DCMD modules.

Mathematical model

LES turbulence model, which applies spatial filtering to the Navier-Stokes equations, is used to investigate the unsteady nature of the flow. The filtered momentum equation for LES model is given by:

$$\frac{\partial \bar{u}_i}{\partial t} + \bar{u}_j \frac{\partial \bar{u}_i}{\partial x_j} = -\frac{1}{\rho}\frac{\partial \bar{p}}{\partial x_i} - \frac{\partial \rho \tau_{ij}}{\partial x_j} + \frac{1}{\rho}\frac{\partial}{\partial x_j}\left(\mu\left(\frac{\partial \bar{u}_i}{\partial x_j} + \frac{\partial \bar{u}_j}{\partial x_i}\right)\right) \quad (21)$$

where *t* represents the time. The subgrid scale stress is given by

$$\tau_{ij} = \overline{u_i u_j} - \bar{u}_j \bar{u}_i$$

Wall-adapting Local Eddy-Viscosity (WALE) is used to capture more details near the membrane walls. More details of WALE subgrid-scale model can be found in [61-63]

The unsteady version of the filtered mass transport and energy equation are used in LES to characterize the concentration and temperature field as

$$\frac{\partial \bar{c}}{\partial t} + \bar{u}_j \frac{\partial \bar{c}}{\partial x_j} = \frac{\partial}{\partial x_j}\left((D + \frac{\mu_t}{\rho\, Sc_t})\frac{\partial \bar{c}}{\partial x_j}\right) \quad (22)$$

$$\frac{\partial \bar{T}}{\partial t} + \bar{u}_j \frac{\partial \bar{T}}{\partial x_j} = \frac{\partial}{\partial x_j}\left((\frac{k_f}{\rho c_p} + \frac{\mu_t}{\rho\, Pr_t})\frac{\partial \bar{T}}{\partial x_j}\right) \quad (23)$$

Results

Fig. 29 shows contours of the normalized concentration, temperature, wall shear stress, and suction rate along the membrane surface at the feed side for $23 \leq x/h \leq 47$. Fig. 29 (a), (c), (e), and (g) represent the contours obtained by k-ω SST simulation while Fig. 29 (b), (d), (f), and (h) illustrate images obtained by LES simulation. Time is normalized as

$$\alpha = t\, U_{ave}/d_s$$

where d_s is the spacer diameter. The instantaneous contours were rendered at $\alpha = 28$. Fig. 29 (a) and (b) show the contours of the normalized concentration over the surface of the membrane at the feed side for steady state and transient simulations. The concentration

was normalized with the inlet feed concentration. Patterns of high and low concentration regions are observed over the membrane surface succeeding the spacer cells for both steady and transient simulations. The instantaneous contours of the concentration, temperature, wall shear stress and the suction rate depict more irregular patterns induced by small-scale eddies observed in the transient simulations. The normalized temperature contour is slightly improved in the transient simulations. The streaks of low temperature regions predicted by steady k-w SST model is seen in Fig. 29 (c). The patterns of the low temperature streaks become more irregular but more importantly the temperature is increased, as illustrated in Fig. 29(d). This implies that mixing predicted by the LES model is more intense and the predicted intensity of the temperature polarization is less. Fig 29 (e) and (f) show the contours of normalized wall shear stress over the membrane surface. The shear stress was normalized with the maximum shear stress. The low shear stress regions seen behind the intersection of strands. The low shear stress regions seen behind the intersection of strands corresponds to the low temperature and high concentration regions as depicted in the concentration and temperature contours. The effects of transient flow in Fig. 29 (f) is clear especially in the downstream of spacers; transient effects aid in reducing low shear regions. Fig. 29 (g) and (h) show the water flux along the membrane surface. The water flux was normalized with the pure water permeability and the vapor pressure difference determined at the inlet temperature of the feed and the permeate solution. The repeated patterns of low and high-flux regions are disrupted and the flux distribution becomes more uniform by the transient effect. The averaged area flux obtained was $89.22\ and\ 90.77\ kg/m^2h$ for steady state and transient simulations, respectively.

The improved temperature and concentration polarization is reflected in the increase of the module-averaged flux.

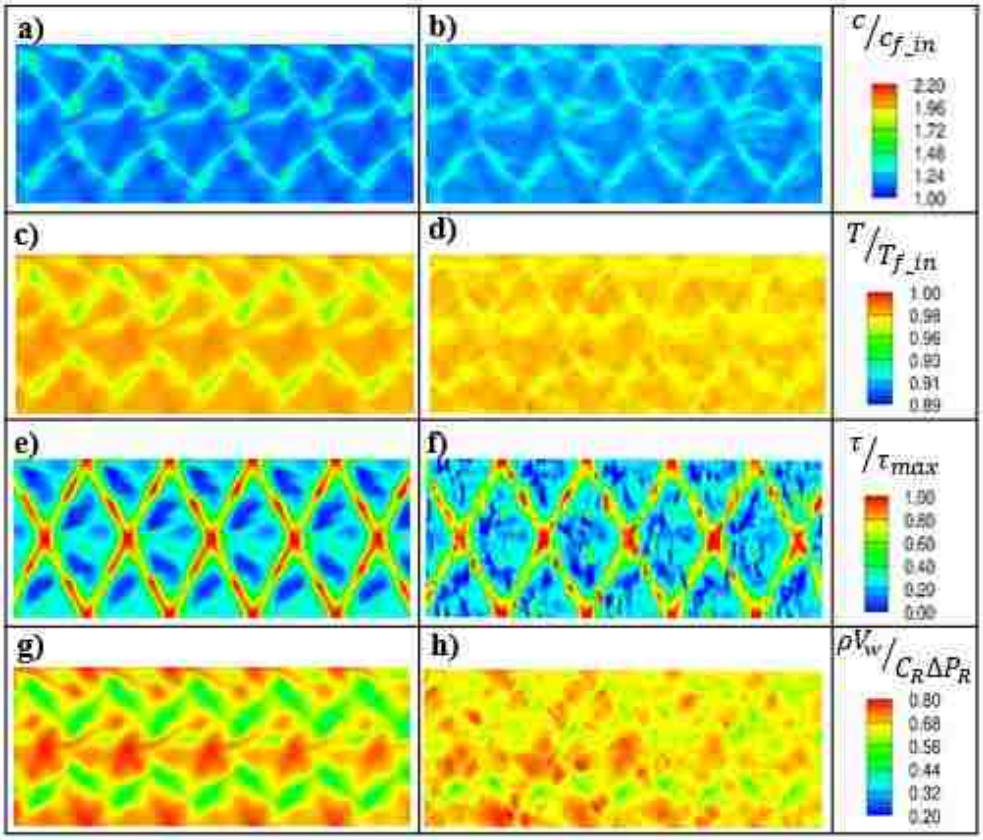

Figure 29. Contours of a) normalized feed concentration for steady flow b) normalized feed concentration for transient flow at α =28, c) normalized feed temperature for steady flow d) normalized feed temperature for transient flow at α =28, e) normalized feed wall shear stress for steady flow f) normalized feed wall shear stress for transient flow at α =28 g) normalized water flux for steady flow h) normalized water flux for transient flow at α =28.

Fig. 30 depicts the iso-surfaces of the Q-criterion for the steady state and transient simulations. The Q-criterion contours rendered inside the feed channel. The iso-surface obtained by the steady state simulation and the instantaneous iso-surface at α = 28 are displayed in Fig. 30. Instantaneous images show that the flow pattern is not regular. The vortical activities is denser as shown in the instantaneous iso-surfaces. The vortical activities in this configuration help to create mixing in the bulk and generate more uniform

distribution of the temperature, concentration, wall shear and flux over the membrane surface.

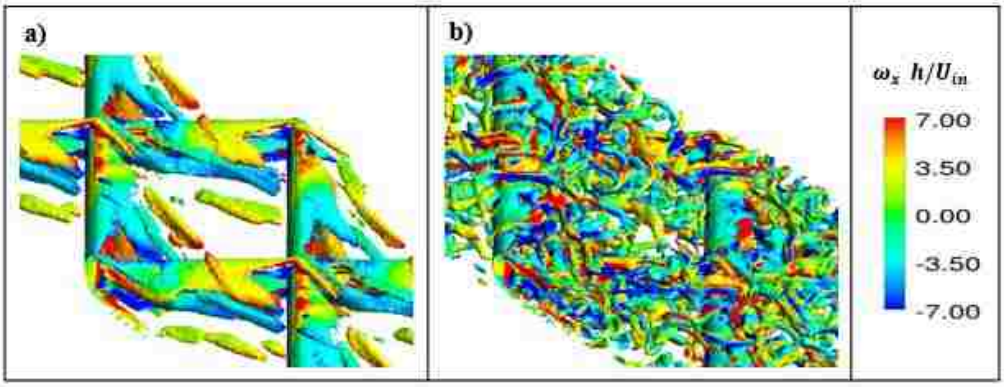

Figure 30. Contours of Iso-surfaces of the Q criterion at level 0.06 of the feed channel for a) steady flow b) transient flow at α=28.

Fig. 31 shows the instantaneous contours of the normalized concentration, temperature, wall shear stress, and suction rate along the membrane surface at the feed side at instant α = 42. The structure of flow over contours in Fig. 31 is comparable to instantaneous contours at α = 28 in Fig. 29. The irregular structure can be seen over the membrane surface for the water flux where the regular patterns in Fig. 29 (g) is disrupted by the transient flow. The averaged area flux obtained at α = 48 is similar to flux obtained at α = 28; implying the velocity, concentration and temperature field are not strongly time-dependent.

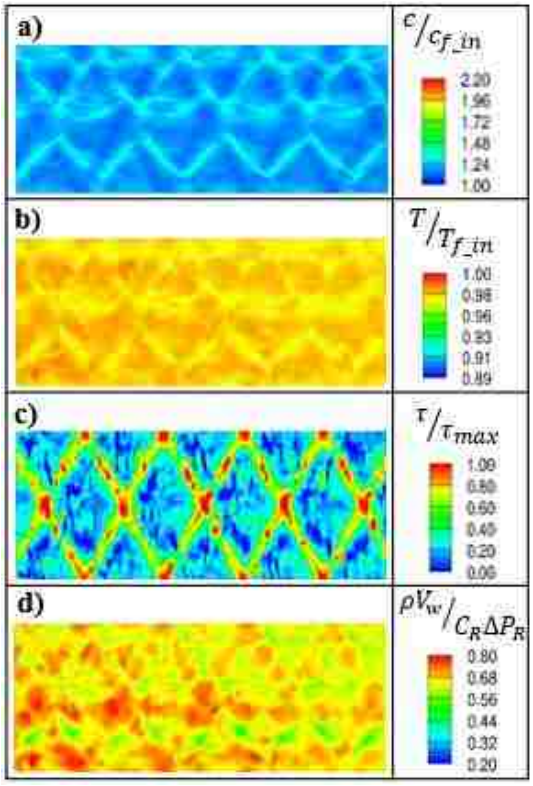

Figure 31. Contours of a) normalized feed concentration, b) normalized feed temperature, c) normalized feed wall shear stress, d) normalized water flux. All transient flow at α = 42

Conclusion

In this study, steady state and transient simulations are conducted to characterize the flow, concentration, and temperature field in DCMD module. Net-type spacers with 45° angle are used in the feed and permeate bulk. Spacers with strand diameter of $0.5h$, where h is the high of ethier feed or permeate channel, was used. Vapor water flux through the membrane is modeled using a Dusty-Gas model where the permeation rate is coupled along the membrane surface with local feed concentration and local feed and permeate temperature. The k-ω SST turbulence model is used for steady state simulation while the LES model is used for transient simulation. The feed Reynolds number was 1500 while it is 330 for the permeate channel. The inlet feed and permeate temperature is set to 353 K

and $293\ K$, respectively. The LES simulations predict the intensity of the temperature and concentration polarization to be less compared to that predicted by the steady state simulations. The transient simulations predict that better mixing in the module, and thus flow properties have more uniform distribution over the membrane surface. The module-averaged water permeation rate predicted by the k-ω SST turbulence model is only 2% less than the flux obtained by LES turbulence model; validating the use of k-ω SST model to simulate the separation process in these modules.

Chapter 7: Conclusion

Computational fluid dynamics simulations were used to study DCMD systems under different scenarios. The continuity, momentum, energy, and mass transport equations were used to model the variation of flow properties in the DCMD system. In empty channels, the laminar model was used. In channels containing turbulent promoters, the $k-\omega$ SST and LES turbulence model was implemented. The Dusty-Gas model is used to describe the mass diffusion through the membrane. The membrane surface is treated as a functional surface where the water vapor flux is coupled with the feed temperature, permeate temperature, and feed concentration. The membrane permeability, determined based on the Knudsen and molecular diffusion, is taken as a function of both membrane properties and the operational parameters. The results obtained by $k-\omega$ SST turbulence model was compared against results obtained by the high fidelity LES turbulence model in a module containing a net type of spacers in the feed channel for a selected set of operational and membrane parameters. Results obtained by both turbulence model agree within less than 2% deviation; validating the $k-\omega$ SST turbulence model and demonstrating that both turbulence model captures transport phenomena in these systems. The mathematical model was also validated against existing experimental work found in the literature with good agreement.

In membrane distillation systems, the temperature polarization is the main reason for reducing the vapor pressure difference across the membrane. The temperature polarization along the surface of the membrane occurs due to the heat transfer from the feed to permeate solution by conduction and enthalpy of vaporization/condensation of the vapor transferred

across the membrane. As a result, the thermal boundary layer forms at each side of the membrane. Like other membrane desalination systems, the solute accumulates on the membrane surface at the feed side as the water vapor permeates through the membrane causes the concentration polarization.

A parametric study was conducted to assess the effect of membrane properties and the effect of the feed operational parameters. Simulations were carried out in an empty flat sheet module by employing the laminar flow model. The thickness of the membrane was varied as $100\ \mu m$, $130\ \mu m$, and $170\ \mu m$. The porosity of the membrane was varied as 0.6, 0.7, and 0.8. Also, the pore size was chosen as $0.2\ \mu m$, $0.45\ \mu m$, and $1\ \mu m$. The water vapor flux increased by 26% when the membrane thickness reduced from 170 to $100\ \mu m$ at fixed porosity and pore size at 0.8 and $0.45\ \mu m$. However, the temperature polarization coefficient decreased by 28% and the concentration polarization coefficient increased by 13% at the same membrane properties. The results indicate that the optimum membrane properties were chosen as, the membrane thickness of $100\ \mu m$, the porosity of 0.8, and the pore size of $0.45\ \mu m$. The feed inlet temperature was varied as 50 ℃, 60 ℃, 70 ℃, and 80 ℃. The feed flow rate was varied as Re_f of 100, 500, 1000, and 1500. The water vapor flux increases exponentially with increasing the inlet feed temperature. The flux increased from 19 to 59 $kg\ m^{-2}h^{-1}$ when the inlet feed temperature increased from 50 to 80 ℃ at Re_f = 1500, while the average temperature polarization coefficient decreased by 26%. The average concentration polarization coefficient at the same condition increased by 53%. The increased feed flow rate improves the temperature and concentration polarization, but the polarization mitigation is limited when the flow regime in channels is laminar. The maximum flux obtained in this study was 64 $kg\ m^{-2}h^{-1}$ at membrane thickness of

$100\ \mu m$, the porosity of 0.8, the pore size of $1\ \mu m$, the inlet feed temperature of 80 ℃, and feed Reynolds number of 1500.

The temperature and concentration polarization have adverse effects on the unit performance. The net-type spacers of 45° angle placed in the middle of the channel to promote mixing and thus to mitigate polarizations. The net-type spacer diameter was set to $d_s = 0.25h$ and $d_s = 0.5h$. The flow rate of the feed channel was varied as Re_f = 500 and 1500. The inlet temperatures for the feed and permeate stream were set to 80 ℃ and 20 ℃, respectively. The water vapor flux was enhanced by 52% by using a spacer diameter of $d_s = 0.5h$ and the Re_f = 1500 compared with the empty channel. increasing the spacer's diameter from $0.25h$ to $0.5h$ enhanced the flux by 12.5%. The results demonstrated that the spacers become more efficient at a high feed flow rate. The results indicate that both the concentration polarization was mitigated while the temperature polarization suffer especially in the permeate channel.

The spacers embedded membrane, a novel design, is proposed to promote mixing near the membrane surface and that in turn to alleviate temperature and concentration polarization. This unique design is realized by placing a net type of spacers between active layers. It could be one of the ideal solutions for these separation units since mixing is local the induced pressure losses would be reduced significantly. The embedded spacers diameter of $D = 0.1h$, $D = 0.2h$, and $D = 0.3h$, the feed flow rate of Re_f = 500 and 1500, and the permeate flow rate of Re_p 330 and 1500 were considered in the study. The inlet temperatures for feed and permeate channel were set to 80 ℃ and 20 ℃, respectively. The inlet concentration of the feed water was taken as $0.035\ [\mathrm{kg_{solute}}/\mathrm{kg_{water}}]$ representing

a typical seawater desalination process. The results indicate the embedded spacers is more efficient at high flow rates and large spacer's diameter. The water vapor flux was enhanced by 39.46% with $D = 0.3h$, Re_f = 1500, and Re_p = 1500 where it is only 3.8% with $D = 0.1h$, Re_f = 500, and Re_p = 330 compared with an empty channel. Embedded spacers effectively mitigate the concentration polarization at all flow rates and spacer diameter. The reason is that the concentration boundary layer is thin, and the embedded spacers managed to disrupt the small concentration boundary layer. Temperature polarization coefficient improved by 39.2% by increasing Re_p from 330 to 1500 at Re_f = 1500 and $D = 0.3h$. It is shown that the mitigation of temperature polarization requires high flow rates in both channels.

From the results of the current work, it is recommended that more research is to be conducted in DCMD systems. The tortuosity of the membrane is an important property which was not studied. Also, the ability of DCMD to treat a high level of concentration in the feed channel needs to be investigated. The membrane shape and its properties play an important role in the DCMD system. Therefore, fabricating the membrane allow us to control the membrane properties and introduce a design that has an ability to create a better mixing near the membrane surface. The embedded spacers offer a significant enhancement of water vapor flux, a reduction of concentration and temperature polarization. Therefore, the optimization study could add more value to this innovative design. Moreover, embedded spacers can be used both as a mixing promoter and as a heat source in the feed and a heat sink in the permeate channel for scale-up systems. It may not be necessary to heat the bulk of the feed but rather only the layer adjacent to the membrane surface.

References

[1] I.C. Karagiannis, P.G. Soldatos, Water desalination cost literature: review and assessment, Desalination. 223 (2008) 448–456.

[2] K.P. Lee, T.C. Arnot, D. Mattia, A review of reverse osmosis membrane materials for desalination — Developmen to date and future potential, J. Memb. Sci. 370 (2010) 1–22. doi:10.1016/j.memsci.2010.12.036.

[3] B.L. Pangarkar, S.K. Deshmukh, V.S. Sapkal, R.S. Sapkal, Review of membrane distillation process for water purification, Desalin. Water Treat. 57 (2016) 2959–2981. doi:10.1080/19443994.2014.985728.

[4] K. Zhani, K. Zarzoum, H. Ben Bacha, J. Koschikowski, D. Pfeifle, Autonomous solar powered membrane distillation systems: state of the art, Desalin. Water Treat. 57 (2016) 23038–23051. doi:10.1080/19443994.2015.1117821.

[5] J. Zhang, N. Dow, M. Duke, E. Ostarcevic, J. De Li, S. Gray, Identification of material and physical features of membrane distillation membranes for high performance desalination, J. Memb. Sci. 349 (2010) 295–303. doi:10.1016/j.memsci.2009.11.056.

[6] A.M. Alklaibi, N. Lior, Membrane-distillation desalination: Status and potential, Desalination. 171 (2005) 111–131. doi:10.1016/j.desal.2004.03.024.

[7] M.S. El-Bourawi, Z. Ding, R. Ma, M. Khayet, A framework for better understanding membrane distillation separation process, J. Memb. Sci. 285 (2006) 4–29. doi:10.1016/j.memsci.2006.08.002.

[8] S. Adnan, M. Hoang, H. Wang, Z. Xie, Commercial PTFE membranes for membrane distillation application: Effect of microstructure and support material, Desalination. 284

(2012) 297–308. doi:10.1016/j.desal.2011.09.015.

[9] H. Hayer, O. Bakhtiari, T. Mohammadi, Simulation of momentum, heat and mass transfer in direct contact membrane distillation: A computational fluid dynamics approach, J. Ind. Eng. Chem. 21 (2015) 1379–1382. doi:10.1016/j.jiec.2014.06.009.

[10] J.-M. Li, Z.-K. Xu, Z.-M. Liu, W.-F. Yuan, H. Xiang, S.-Y. Wang, Y.-Y. Xu, Microporous polypropylene and polyethylene hollow fiber membranes. Part 3. Experimental studies on membrane distillation for desalination, Desalination. 155 (2003) 153–156. doi:10.1016/S0011-9164(03)00292-3.

[11] L. Francis, N. Ghaffour, A.S. Alsaadi, S.P. Nunes, G.L. Amy, Performance evaluation of the DCMD desalination process under bench scale and large scale module operating conditions, J. Memb. Sci. 455 (2014) 103–112. doi:10.1016/j.memsci.2013.12.033.

[12] D. Park, E. Norouzi, C. Park, Experimental and Numerical Study of Water Distillation Performance of Small-Scale Direct Contact Membrane Distillation System, Int. Mech. Eng. Congr. Expo. 8 (2017) 1–9.

[13] S. Soukane, M.W. Naceur, L. Francis, A. Alsaadi, N. Ghaffour, Effect of feed flow pattern on the distribution of permeate fluxes in desalination by direct contact membrane distillation, Desalination. 418 (2017) 43–59. doi:10.1016/j.desal.2017.05.028.

[14] R. Bouchrit, A. Boubakri, A. Hafiane, S.A.T. Bouguecha, Direct contact membrane distillation: Capability to treat hyper-saline solution, Desalination. 376 (2015) 117–129. doi:10.1016/j.desal.2015.08.014.

[15] H.J. Hwang, K. He, S. Gray, J. Zhang, I.S. Moon, Direct contact membrane distillation (DCMD): Experimental study on the commercial PTFE membrane and modeling, J. Memb.

Sci. 371 (2011) 90–98. doi:10.1016/j.memsci.2011.01.020.

[16] J. Phattaranawik, R. Jiraratananon, A.G. Fane, Effects of net-type spacers on heat and mass transfer in direct contact membrane distillation and comparison with ultrafiltration studies, J. Memb. Sci. 217 (2003) 193–206. doi:10.1016/S0376-7388(03)00130-3.

[17] A. Cipollina, G. Micale, L. Rizzuti, Membrane distillation heat transfer enhancement by CFD analysis of internal module geometry, Desalin. Water Treat. 25 (2011) 195–209. doi:10.5004/dwt.2011.1455.

[18] Y. Yun, J. Wang, R. Ma, A.G. Fane, Effects of channel spacers on direct contact membrane distillation, Desalin. Water Treat. 34 (2011) 63–69. doi:10.5004/dwt.2011.2870.

[19] Y.M. Manawi, M.A.M.M. Khraisheh, A.K. Fard, F. Benyahia, S. Adham, A predictive model for the assessment of the temperature polarization effect in direct contact membrane distillation desalination of high salinity feed, Desalination. 341 (2014) 38–49. doi:10.1016/j.desal.2014.02.028.

[20] H. Chang, J.A. Hsu, C.L. Chang, C.D. Ho, T.W. Cheng, Simulation study of transfer characteristics for spacer-filled membrane distillation desalination modules, Appl. Energy. 185 (2017) 2045–2057. doi:10.1016/j.apenergy.2015.12.030.

[21] A. Kayvani Fard, Y.M. Manawi, T. Rhadfi, K.A. Mahmoud, M. Khraisheh, F. Benyahia, Synoptic analysis of direct contact membrane distillation performance in Qatar: A case study, Desalination. 360 (2015) 97–107. doi:10.1016/j.desal.2015.01.016.

[22] J. Seo, Y. Mi, J. Ha, Spacer optimization strategy for direct contact membrane distillation :Shapes, configurations, diameters, and numbers of spacer filaments, 417 (2017) 9–18. doi:10.1016/j.desal.2017.05.009.

[23] A. Katsandri, A theoretical analysis of a spacer filled flat plate membrane distillation modules using CFD: Part I: velocity and shear stress analysis, Desalination. 408 (2017) 145–165. doi:10.1016/j.desal.2015.09.001.

[24] A. Katsandri, A theoretical analysis of a spacer fi lled fl at plate membrane distillation modules using CFD : Part II : Temperature polarisation analysis, Desalination. 408 (2017) 166–180. doi:10.1016/j.desal.2015.11.021.

[25] Y. Taamneh, K. Bataineh, Improving the performance of direct contact membrane distillation utilizing spacer-filled channel, Desalination. 408 (2017) 25–35. doi:10.1016/j.desal.2017.01.004.

[26] Y.D. Kim, L. Francis, J.G. Lee, M.G. Ham, N. Ghaffour, Effect of non-woven net spacer on a direct contact membrane distillation performance: Experimental and theoretical studies, J. Memb. Sci. 564 (2018) 193–203. doi:10.1016/j.memsci.2018.07.019.

[27] H. Yu, X. Yang, R. Wang, A.G. Fane, Analysis of heat and mass transfer by CFD for performance enhancement in direct contact membrane distillation, J. Memb. Sci. 405–406 (2012) 38–47. doi:10.1016/j.memsci.2012.02.035.

[28] M. Usta, A.E. Anqi, A. Oztekin, Reverse osmosis desalination modules containing corrugated m

embranes – Computational study, Desalination. 416 (2017) 129–139. doi:10.1016/j.desal.2017.05.005.

[29] A.M. Alshwairekh, A.A. Alghafis, A.M. Alwatban, U.F. Alqasair, A. Oztekin, The effect of membrane and channel corrugation in forward osmosis membrane modules - Nummerical analyses, Desalination. 460 (2019) 41-55. doi:10.1016/j.desal.2019.03.003

[30] H. Yu, X. Yang, R. Wang, A. Fane, Numerical simulation of heat and mass transfer in direct contact membrane distillation in a hollow fiber module with laminar flow, Vuir.Vu.Edu.Au. (2014) 1–30. http://vuir.vu.edu.au/25291/1/3-Numerical simulation of heat and mass transfer in direct membrane distillation in a hollow fiber module with laminar flow-text.pdf.

[31] Mabrouk A, Elhenawy Y, Moustafa G, Experimental Evaluation of Corrugated Feed Channel of Direct Contact Membrane Distillation, J. Membr. Sci. Technol. 6 (2016). doi:10.4172/2155-9589.1000151.

[32] I. Hitsov, T. Maere, K. De Sitter, C. Dotremont, I. Nopens, Modelling approaches in membrane distillation: A critical review, Sep. Purif. Technol. 142 (2015) 48–64. doi:10.1016/j.seppur.2014.12.026.

[33] S. Mostafa H, J.H.L. V, S.M. Zubair, The thermophysical properties of seawater : A review of existing correlations and data, Desalin. Water Treat. 16 (2013) 1–67.

[34] A.S. Alsaadi, N. Ghaffour, J.D. Li, S. Gray, L. Francis, H. Maab, G.L. Amy, Modeling of air-gap membrane distillation process: A theoretical and experimental study, J. Memb. Sci. 445 (2013) 53–65. doi:10.1016/j.memsci.2013.05.049.

[35] F.R. Menter, Two-equation eddy-viscosity turbulence models for engineering applications, AIAA J. 32 (1994) 1598–1605. doi:10.1016/0029-554X(80)90461-9.

[36] K.W. Lawson, D.R. Lloyd, Membrane distillation, J. Memb. Sci. 124 (1997) 1–25. doi:10.1016/S0376-7388(96)00236-0.

[37] M. Khayet, Membranes and theoretical modeling of membrane distillation: A review, Adv. Colloid Interface Sci. 164 (2011) 56–88. doi:10.1016/j.cis.2010.09.005.

[38] J. Amigo, R. Urtubia, F. Suárez, Exploring the interactions between hydrodynamics and fouling in membrane distillation systems – A multiscale approach using CFD, Desalination. 444 (2018) 63–74. doi:10.1016/j.desal.2018.07.009.

[39] A. Alkhudhiri, N. Darwish, N. Hilal, Membrane distillation: A comprehensive review, Desalination. 287 (2012) 2–18. doi:10.1016/j.desal.2011.08.027.

[40] M. Qtaishat, T. Matsuura, B. Kruczek, M. Khayet, Heat and mass transfer analysis in direct contact membrane distillation, Desalination. 219 (2008) 272–292. doi:10.1016/j.desal.2007.05.019.

[41] J. Phattaranawik, R. Jiraratananon, A.G. Fane, Effect of pore size distribution and air flux on mass transport in direct contact membrane distillation, J. Memb. Sci. 215 (2003) 75–85. doi:10.1016/S0376-7388(02)00603-8.

[42] A. Alkhudhiri, N. Darwish, N. Hilal, Membrane distillation: A comprehensive review, Desalination. 287 (2012) 2–18. doi:10.1016/j.desal.2011.08.027.

[43] J. Phattaranawik, R. Jiraratananon, A.. Fane, Heat transport and membrane distillation coefficients in direct contact membrane distillation, J. Memb. Sci. 212 (2003) 177–193. doi:10.1016/S0376-7388(02)00498-2.

[44] A.G. Fane, R.W. Schofield, C.J.D. Fell, The efficient use of energy in membrane distillation, Desalination. 64 (1987) 231–243. doi:10.1016/0011-9164(87)90099-3.

[45] A.E. Anqi, M. Usta, M. Alrehili, N. Alkhamis, A. Oztekin, Reverse Osmosis Desalination Module: Three Dimensional, Transient Analyses, Int. Mech. Eng. Congr. Expo. (2016) 1–8. doi:10.1115/IMECE2016-65890.

[46] A. Alshwairekh, A. Alghafis, M. Usta, A. Alwatban, R. Krysko, A. Oztekin, The Effect of

Porous Support Layer in Forward Osmosis Membranes – A Computational Fluid Dynamics Simulation, Int. Mech. Eng. Congr. Expo. 7 (2018) 1–9.

[47] A.E. Anqi, N. Alkhamis, A. Oztekin, Numerical simulation of brackish water desalination by a reverse osmosis membrane, Desalination. 369 (2015) 156–164. doi:10.1016/j.desal.2015.05.007.

[48] H. Yu, X. Yang, R. Wang, A.G. Fane, Numerical simulation of heat and mass transfer in direct membrane distillation in a hollow fiber module with laminar flow, J. Memb. Sci. 384 (2011) 107–116. doi:10.1016/j.memsci.2011.09.011.

[49] S. Wardeh, H.P. Morvan, CFD simulations of flow and concentration polarization in spacer-filled channels for application to water desalination, Chem. Eng. Res. Des. 86 (2008) 1107–1116.

[50] P. Termpiyakul, R. Jiraratananon, S. Srisurichan, Heat and mass transfer characteristics of a direct contact membrane distillation process for desalination, Desalination. 177 (2005) 133–141. doi:10.1016/j.desal.2004.11.019.

[51] M. Usta, R.M. Krysco, A.E. Anqi, A. Alshwairekh, A. Oztekin, The Effect of PTFE Membrane Properties on Vacuum Membrane Distillation Module Performance, Int. Mech. Eng. Congr. Expo. 7 (2018) 1–8.

[52] M.M.A. Shirazi, A. Kargari, M.J.A. Shirazi, Direct contact membrane distillation for seawater desalination, Desalin. Water Treat. 49 (2012) 368–375. doi:10.1080/19443994.2012.719466.

[53] K. He, H.J. Hwang, M.W. Woo, I.S. Moon, Production of drinking water from saline water by direct contact membrane distillation (DCMD), J. Ind. Eng. Chem. 17 (2011) 41–48.

doi:10.1016/j.jiec.2010.10.007.

[54] M.M.A. Shirazi, A. Kargari, D. Bastani, L. Fatehi, Production of drinking water from seawater using membrane distillation (MD) alternative: direct contact MD and sweeping gas MD approaches, Desalin. Water Treat. 52 (2014) 2372–2381. doi:10.1080/19443994.2013.797367.

[55] M.M.A. Shirazi, A. Kargari, M. Tabatabaei, Evaluation of commercial PTFE membranes in desalination by direct contact membrane distillation, Chem. Eng. Process. Process Intensif. 76 (2014) 16–25. doi:10.1016/j.cep.2013.11.010.

[56] X. Yang, H. Yu, R. Wang, A.G. Fane, Optimization of microstructured hollow fiber design for membrane distillation applications using CFD modeling, J. Memb. Sci. 421–422 (2012) 258–270. doi:10.1016/j.memsci.2012.07.022.

[57] A. Boubakri, R. Bouchrit, A. Hafiane, S. Al-Tahar Bouguecha, Fluoride removal from aqueous solution by direct contact membrane distillation: Theoretical and experimental studies, Environ. Sci. Pollut. Res. 21 (2014) 10493–10501. doi:10.1007/s11356-014-2858-z.

[58] G. Naidu, S. Jeong, S. Vigneswaran, T.M. Hwang, Y.J. Choi, S.H. Kim, A review on fouling of membrane distillation, Desalin. Water Treat. 57 (2016) 10052–10076. doi:10.1080/19443994.2015.1040271.

[59] I.S. Al-Mutaz, A.S. Al-Motek, I. Wazeer, Variation of distillate flux in direct contact membrane distillation for water desalination, Desalin. Water Treat. 62 (2017) 86–93. doi:10.5004/dwt.2017.20147.

[60] A. Luo, N. Lior, Study of advancement to higher temperature membrane distillation,

Desalination. 419 (2017) 88–100. doi:10.1016/j.desal.2017.05.020.

[61] USTA, Mustafa, "Computational Study of Desalination be Membranes" (2018). Theses and Dissertations. 4328

[62] F.R. Menter, Two-Equation Eddy-Viscosity Turbulence Models for Engineering Applications, vol. 32, (1994), https://doi.org/10.2514/3.12149.

[63] F. Ducros, F. Nicoud, Subgrid-scale stress modelling based on the square of the velocity gradient tensor, Flow, Turbul. Combust. (1999) 1–36.

VITA

Anas Alwatban was born on May 11 – 1986 in Buraydah Saudi Arabia. He received his Bachelor of Science degree in mechanical engineering from Qassim University in Saudi Arabia in 2010 and joined Qassim University in 2011. He got his Master of Science in Renewable and Clean Energy from the University of Dayton in 2016. Anas returned to work for one year in Qassim University in Saudi Arabia as a lecturer. He taught two lab courses fluid mechanics lab, and heat transfer lab. He will receive the degree of Doctor of Philosophy in mechanical engineering from Lehigh University in 2019.